Structural matching investigation of FPCBBs and CRBs in offshore wind gearbox based on rotor dynamic model

Structural matching investigation of FPCBBs and CRBs in offshore wind gearbox based on rotor dynamic model

Shuaijun Ma[1,2], Lenci Stefano[2], Linbo Zhu*[3], Ke Yan*[1], Haizhen Li[1], Bo Wen[1], Jun Hong[1]

1. Key Laboratory of Education Ministry for Modern Design and Rotor-Bearing System, Xi'an Jiaotong University, 710049 Xi'an, People's Republic of China

2. Department of Civil and Building Engineering and Architecture, Polytechnic University of Marche, 60131 Ancona, Italy

3. School of Chemical Engineering and Technology, Xi'an Jiaotong University, 710049, Xi'an, People's Republic of China

Corresponding author's email address: linbozhu@mail.xjtu.edu.cn, yanke@mail.xjtu.edu.cn

Abstract:

The combination of four-point contact ball bearings (FPCBB) and cylindrical roller bearings (CRB) is widely used in offshore wind gearbox. Improper structural parameters can lead to a significant reduction in gearbox performance, especially clearance. Therefore, this paper presents a new dynamic model of the bearing-rotor system, covering CRBs and FPCBB. The slice method is used to well addressed the difficulty of the non-uniform contact between the rollers and other components. The semi-flexible body element perfectly balances the three aspects: rotor flexibility, real-time coupling, and simultaneous solution of the bearing and rotor models. The differences between the rigid and flexible models in predicting the system behavior are compared. The effect of the bearing clearance on the dynamic performance of the system is further investigated. The results show that the flexible model is capable of predicting stress concentrations in the CRB raceways and multi-point contact state inside FPCBB compared to the rigid model. The CRB clearance has a more significant effect on the system dynamic performance: the wider the CRB clearance, the more pronounced the sliding inside the raceway of the right CRB. The work provides new ideas for modeling and performance optimization of the bearing-rotor system in offshore wind gearbox.

Keywords: four-point contact ball bearing; semi-flexible body element; contact feature; nonlinear dynamic response

1. Introduction

Four-point contact ball bearings (FPCBB), featured with a multiple raceway construction, are frequently specified for the rotating systems with limited design space and demanding requirements, such as offshore wind gearbox [1-3]. To further enhance the service performance, it is necessary to combine them with other bearings [4], in particular cylindrical roller bearings (CRB). Since both types of bearings are sensitive to changes in clearance, the effect of clearance on their dynamic performance should be considered before using such structures [5]. Numerical modeling is required to elucidate this mechanism due to the limitations of experimental testing conditions and impossibility to have analytical solutions. Therefore, there is an urgent need to develop a dynamic

model of the bearing-rotor system covering both FPCBB and CRB.

Since Stribeck first proposed the ball bearing model [6], many mechanical models for the individual bearing have appeared. These models can be subdivided into static models [7-9], quasi-static models [10-12], quasi-dynamic models[13-15] and dynamic models[16-20]. Among them, the dynamic model is widely used in bearing performance studies as most factors are considered. The modeling of angular contact ball bearings has become increasingly sophisticated, while mature models for these two types of bearings have not yet appeared. Fortunately, the dynamic model for FPCBB has been proposed to support the subsequent work [3, 21]. The following discussion would focus on the CRB modeling. Tu [22-24] presented a dynamic model of CRB by restricting the motion of the roller and the inner ring in the radial plane. Subsequently, the dynamic behavior on the roller/raceway interface was investigated under different operating conditions [23]. On this basis, the complex physical parameters of the lubricant inside CRB were considered by Chen [25-27]. The effects of factors such as temperature and viscosity on the sliding behavior inside the bearing were further examined. Regrettably, the degrees of freedom of the moving parts in these models were too low to accurately simulate their motion. The slice method was used by Han [28-29] to improve these models to consider the deflection of the roller and ring. He investigated the time-varying frictional properties of contact interfaces under bias load conditions. However, the nonlinear equations were used to constrain some of the degrees of freedom of these parts inside CRB. Therefore, it was not possible to accurately simulate their dynamic behaviors. Discarding these equations, Deng [30-34] adopted differential equations to determine all motion of each part inside CRB, thus improving the previous model. He further studied the influence of roller unbalance and lubricant on the cage dynamic behavior [32, 34]. There was an important simplification in terms of the contact between the cage and other components. Besides, Liu et al. [35-38] developed a CRB dynamic model with raceway defects and investigated the effect of fault size on bearing vibration. Although continuous improvements have been made to the CRB dynamic model to study its dynamic behavior, these have been conducted based on individual bearings. As mentioned earlier, it is not possible to precisely model the bearing dynamic behavior as the interactions between bearings and bearings or between bearings and system are ignored [39-40].

Numerical simulation model of the bearing-rotor system has been proposed and continuously improved by some scholars [41-55]. The stiffness coupling method was employed by Ma [41-43] to construct a dynamic model of the bearing-rotor system. The overall stiffness matrix of the bearing was obtained by solving the quasi-static model and introduced into the rotor model to obtain the dynamic response of the system. Since the effects of lubricant and cage have been ignored, the dynamic behavior of the system cannot be modeled well [44]. A further improvement of the system model was made by Cao [44-46], who used the bearing dynamic model instead of the quasi-static model. The effectiveness of the model predictions is questionable due to the inconsistency of the solution algorithms for the bearing and rotor models [47]. The same author [47-50] introduced the concept of rigid elements, which enabled real-time coupling and simultaneous solving of the two models. The rotor was discretized into a finite number of elements, and the deformation of the rotor could be simulated by adding springs and damper between these elements. The motion equations for these elements were the same as those for the bearing components and were solved by the same algorithm. However, the stiffness of the springs and damping are too empirical, and the deformation inside the element was ignored [47]. As a result, these models are still unable to accurately simulate the dynamic behavior of the system despite significant improvements.

In conclusion, as far as the bearing dynamic model is concerned, there is lack of detailed consideration of the non-homogeneous contact of the roller with other components. In terms of the bearing-rotor system model, there are no good solutions that consider both the rotor flexibility and the real-time interaction between the two models. Furthermore, the investigation of bearing performance is limited to a single bearing model, without considering the effects of other components in the system. Therefore, taking the input shaft of an offshore wind gearbox as an example, a CRB dynamic mode is proposed in this paper. The non-homogeneous contact between the roller and other components is well addressed by the slice method. Combined with the FPCBB model and semi-flexible element (SFBE) by our team in the early stage [3, 21, 51], a bearing-rotor system model covering FPCBB and CRB is further presented. The differences between rigid and flexible models in predicting the dynamic performance of the system are compared. The influence of different bearing clearances on the dynamic behavior of the system is further investigated.

2. Dynamic modeling of bearing-rotor systems

Figure 1 presents a common bearing-rotor system in offshore wind gearbox, which consists of two CRBs, an FPCBB and a helical gear [52]. During normal operation of the system, the bearings are inevitable subjected to combined axial-radial load from the helical gear. Ideally, CRBs carries the full radial component of this load, while its full axial component is borne by FPCBB. However, in some cases, such as when FPCBB is unable to eliminate the radial component of the load by radial movement, CRBs will inevitably have to take on the axial component. The dynamic performance of the system may be weakened or even damaged as a result. It depends not only on its structural design, but also to a large extent on the interaction mechanism among the individual bearing clearances. A dynamic model of the bearing-rotor system is needed to investigate this mechanism, which is the focus of this section.

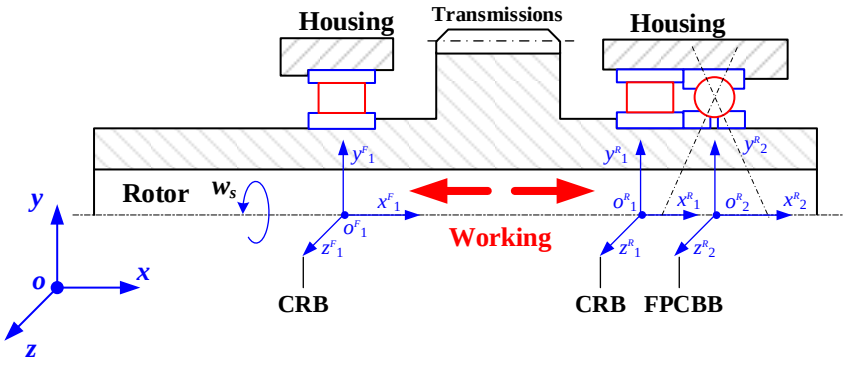

Fig. 1. Sketch of a shaft system consisting of CRBs and FPCBB

2.1 Bearing-rotor system discretization

As shown in **Fig. 1**, the external load of the system is generated by the helical gear and passes sequentially through the rotor, the bearings and the housing. In the process, the rotor deforms as the load is transferred, thus affecting the external load applied to the bearings (especially CRBs). Therefore, the rotor has to be discretized using SFBE to take into account its flexibility. The discretized model of the bearing-rotor system is presented in **Fig. 2**. It consists of two SFBEs, one

with bearings and the other without bearings. Since these two SFBEs have different constraint loads, their differential equations of motion are quite different. Therefore, they need to be modeled separately.

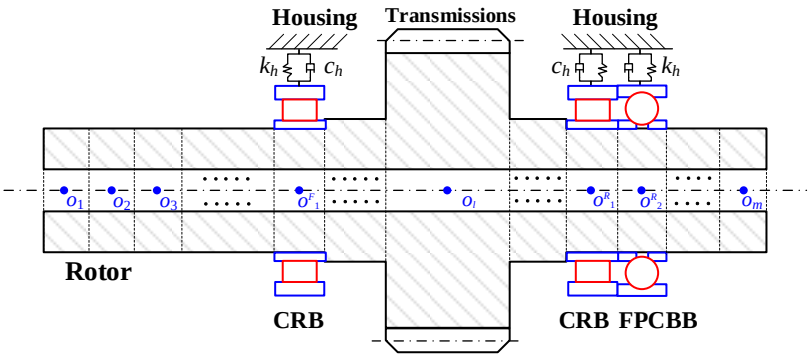

Fig. 2. Discretization of bearing-rotor system based on SFBEs

The SFBEs with bearings are further divided into two categories, one containing FPCBB and the other containing CRB. The modeling method for the former is described in detail in the previously published papers of our group [3, 21]. Therefore, the discussion of this section will focus on the constrained equations of motion for SFBEs with CRB and SFBEs without bearings.

2.2 Dynamic modeling of CRB

The dynamic model for SFBE with CRB includes the definition of the bearing coordinate frame, the interaction between its components, the differential equations of motion, and so on. Each of these will be discussed in this part.

2.2.1 Definition of coordinate frame system

Before determining the interactions between the components in CRB, a larger number of coordinate frames need to be defined to describe their position in space. These coordinate frames are illustrated in **Fig. 3**, including the inertial coordinate frame (o-xyz), the l-th SFBE coordinate frame (o_l-$x_l y_l z_l$), the inner ring coordinate frame (o_{li}-$x_{li}y_{li}z_{li}$), the outer ring coordinate frame (o_{lo}-$x_{lo}y_{lo}z_{lo}$), the housing coordinate frame (o_{lh}-$x_{lh}y_{lh}z_{lh}$), the cage coordinate frame (o_{lc}-$x_{lc}y_{lc}z_{lc}$), the j-th roller coordinate frame (o_{lbj}-$x_{lbj}y_{lbj}z_{lbj}$), and the j-th pocket coordinate frame (o_{lcj}-$x_{lcj}y_{lcj}z_{lcj}$). Since the SFBE of the rotor is fixed to the CRB inner ring, it is considered as the inner ring coordinate frame (o_{li}-$x_{li}y_{li}z_{li}$). Importantly, it is necessary to establish an azimuthal coordinate system (o_{laj}-$x_{laj}y_{laj}z_{laj}$) for the roller so that its position relative to other components can be easily determined.

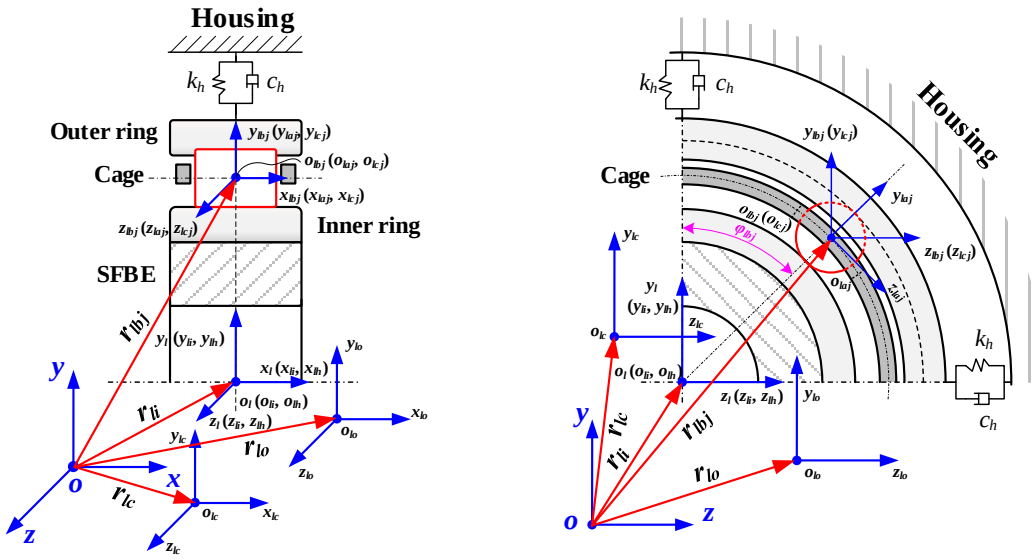

(a) (b)

Fig. 3. Coordinate frame system of CRB: (a) axial section; (b)Radial section

2.2.2 Interaction between the roller and raceways

The interaction between the roller and raceways is detailed in **Fig. 4**. Since the load vector applied to CRB may contain axial load, moments, etc., it can lead to serious non-uniformity in the stress distribution between them along the roller generatrix. It is therefore necessary to divide the roller into a certain number of small slices and then calculate the forces between each slice and the raceway. By superimposing these forces, the interaction force between them can be obtained, known as the slicing method.

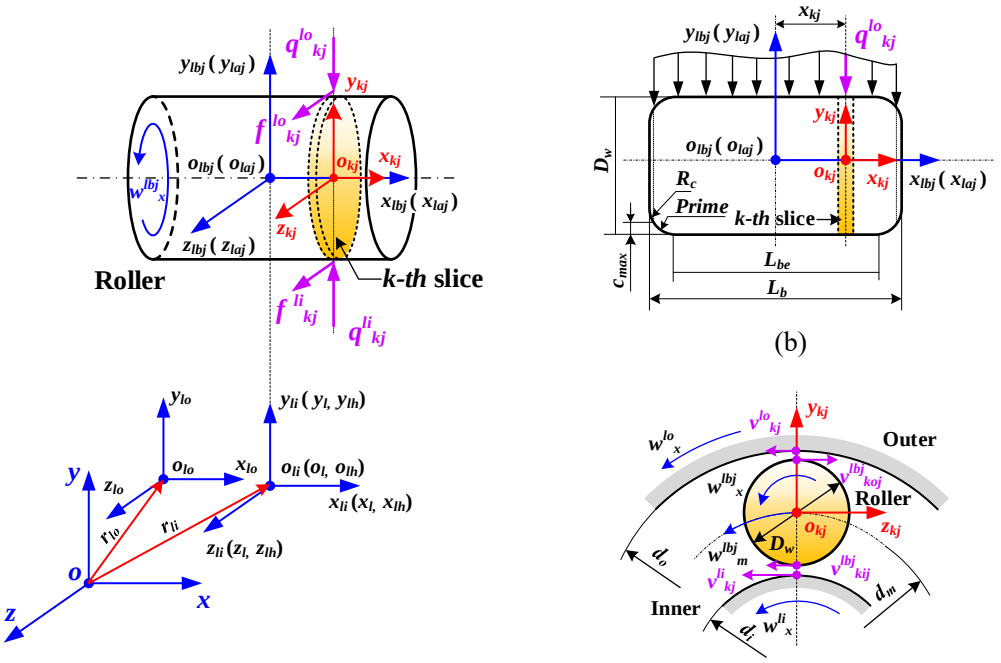

(a) (b) (c)

Fig. 4. Interaction between the roller and raceway based on the slicing method; (a) spatial geometry

relationship; (b) stress distribution on roller; (c) force exerted on *k*-th slice.

As shown in **Figs. 4(a)** and **4(b)**, for any slice (*k*-th slice, for example), its position vector in the roller azimuthal coordinate frame can be expressed as:

$$r_{kj}^{laj} = \begin{bmatrix} x_{kj} & 0 & 0 \end{bmatrix}^T = \left[\left(-0.5 + \frac{k+0.5}{n} \right) \cdot L_b \quad 0 \quad 0 \right]^T \tag{1}$$

where k is the number of the slice, $k = 1, 2, 3, \cdots, n$. n denotes the total number of slices. L_b represents the roller length.

Before determining the forces on this slice, it is necessary to obtain its position vector in the inner ring coordinate system.

$$r_{kj}^{li} = \left[T_{li} \right] \cdot \left(r_{lbj} - r_{li} \right) + \left[T_{lbj}^{li} \right]^{-1} \left[T_{laj}^{lbj} \right]^{-1} \cdot r_{kj}^{laj} \tag{2}$$

where $\boldsymbol{r_{lbj}}$ is the position vector of the *j*-th roller, and $\boldsymbol{r_{li}}$ is the position vector of the inner ring. T_{li} denotes the transformation matrix from the inertial coordinate frame to the inner ring coordinate frame, T^{li}_{lbj} represents the transformation matrix from the inner ring coordinate frame to the *j*-th roller coordinate frame, and T^{lbj}_{laj} represents the transformation matrix from the *j*-th roller coordinate frame to its azimuthal coordinate frame.

The interpenetration between this slice and the inner raceway is further determined as follows:

$$\delta_{kj}^{li} = \left\{ \left(d_i + D_w \right)/2 - \left[\left(y_{kj}^{li\,2} + z_{kj}^{li\,2} \right)^{0.5} - c_k \right] \quad 0 \right\}_{\max} \tag{3}$$

where d_i is the diameter of the inner raceway, and D_w is the roller diameter. c_k denotes the parameters for roller profiling, defined by:

$$c_k = \begin{cases} c_{\max} \left\{ \dfrac{\left[\left(2k-n-1 \right)/n \right]^2 - \left(L_{be}/L_b \right)^2}{1 - L_{be}/L_b} \right\} & \left[\left(2k-n-1 \right)/n \right]^2 - \left(L_{be}/L_b \right)^2 > 0 \\ 0 & \left[\left(2k-n-1 \right)/n \right]^2 - \left(L_{be}/L_b \right)^2 \le 0 \end{cases} \tag{4}$$

where $c_{\max}$ is the maximum convexity of the roller, and L_{be} is the roller length without profiling.

According to Hertz's theory, the contact load between this slice and the inner raceway can be defined as:

$$q_{kj}^{li} = \frac{L_b E_1 E_2}{1.319 \cdot n L_{be}^{0.11} \left[E_2 \left(1 - v_1^2 \right) + E_1 \left(1 - v_2^2 \right) \right]} \cdot \delta_{kj}^{li1.11} \tag{5}$$

where v and E are the Poisson's ratio and Young's modulus of the material, respectively.

As shown in **Fig. 4(c)**, in addition to the contact load, the *k*-th slice is subjected to friction due to relative motion with raceway. Since the friction force is determined by velocity and load, it is necessary to obtain the velocity vector between them. The absolute velocity of the inner raceway at their contact point is expressed as:

$$v_{kj}^{li} = w_x^{li} \cdot d_i/2 - w_y^{li} \cdot x_{kj} + w_m^{li} \left(y_{li}^2 + z_{li}^2 \right)^{0.5} \tag{6}$$

where w^{li} is the angular velocity of the inner ring in the inertial coordinate frame. w^{li}_m is the revolution speed around the rotor axis, obtained by:

$$w_m^{li} = -v_y^{li} \cdot z_{li} \Big/ \left(y_{li}^2 + z_{li}^2 \right) + v_z^{li} \cdot y_{li} \Big/ \left(y_{li}^2 + z_{li}^2 \right) \tag{7}$$

where v^{li} is the displacement of the inner ring in the inertial coordinate frame.
Similarly, the absolute velocity of the k-th slice at this point is obtained by:

$$v_{kij}^{lbj} = w_x^{lbj} \cdot D_w/2 - w_y^{lbj} \cdot x_{kj} + w_m^{lbj} \left(y_{lbj}^2 + z_{lbj}^2 \right)^{0.5} \tag{8}$$

where w^{lbj} is the angular velocity of the j-th roller in the inertial coordinate frame.
The rolling and sliding velocities between the k-th slice and the inner raceway can be expressed respectively as:

$$\begin{cases} u_{kj}^{li} = \left| v_{kj}^{li} + v_{kij}^{lbj} \right| / 2 \\ \Delta v_{kj}^{li} = -v_{kj}^{li} + v_{kij}^{lbj} \end{cases} \tag{9}$$

Considering the effect of the lubricant, the friction force between them can be further determined as [32]:

$$f_{kj}^{li} = q_{kj}^{li} \cdot \left[\left(A + B \cdot \left| \Delta v_{kj}^{li} \right| / u_{kj}^{li} \right) e^{C \cdot \left| \Delta v_{kj}^{li} \right| / u_{kj}^{li}} + D \right] \cdot sign\left(\Delta v_{kj}^{li} \right) \tag{10}$$

where A, B, C, and D are lubricant-related coefficients, determined by many parameters such as velocity, pressure and lubricant viscosity.
Similar to the inner raceway, the interaction force between the k-th slice and the outer raceway can be found in the same way. All these forces acting on the slices are converted to the roller center and then summed to further derive the force vector applied on the j-th roller.

$$F_{bj}^{lr} = \begin{bmatrix} \left[T_{lbj} \right]^{-1} & 0 \\ 0 & \left[T_{lbj} \right]^{-1} \end{bmatrix} \begin{bmatrix} \left[T_{laj}^{lbj} \right]^{-1} & 0 \\ 0 & \left[T_{laj}^{lbj} \right]^{-1} \end{bmatrix} \begin{bmatrix} 0 \\ \sum_{k=1}^{n} \left(q_{kj}^{li} - q_{kj}^{lo} \right) \\ \sum_{k=1}^{n} \left(f_{kj}^{li} + f_{kj}^{lo} \right) \\ \sum_{k=1}^{n} \left(-f_{kj}^{li} + f_{kj}^{lo} \right) \cdot D_w/2 \\ \sum_{k=1}^{n} \left(-f_{kj}^{li} - f_{kj}^{lo} \right) \cdot x_{kj} \\ \sum_{k=1}^{n} \left(q_{kj}^{li} - q_{kj}^{lo} \right) \cdot x_{kj} \end{bmatrix} \tag{11}$$

where T_{lbj} represents the transformation matrix from the inertial coordinate frame to the j-th roller coordinate frame.

2.2.3 External loads on the cage

The excitation loads exerted on the cage come mainly from the rollers and the guiding ring, which is discussed in detail in this part. **Figure 5** presents the interaction forces between the cage pocket and the roller. Similar to the stresses on the raceway, the stress distribution between the roller and pocket is very heterogeneous, which also needs to be obtained using the slicing method. As shown in **Figs. 5(a)** and **5(b)**, the position vector of the k-th slice in the pocket coordinate system with respect to the pocket center can be expressed as:

$$r_{kj}^{lcj}=\left[T_{lcj}^{lc}\right]\left\{\left[T_{lc}\right]^{-1}\left(r_{lbj}+\left[T_{lbj}\right]^{-1}\left[T_{laj}^{lbj}\right]^{-1}r_{kj}^{laj}-r_{lc}\right)-r_{cj}^{lc}\right\} \tag{12}$$

where $\boldsymbol{r_{lc}}$ is the position vector of the cage, and $\boldsymbol{r}^{lc}_{cj}$ is the position vector of the j-th pocket in the cage coordinate frame. T_{lc} is the transformation matrix from the inertial coordinate frame to the cage coordinate frame, and T^{lc}_{lcj} is the transformation matrix from the cage coordinate frame to the j-th pocket coordinate frame.

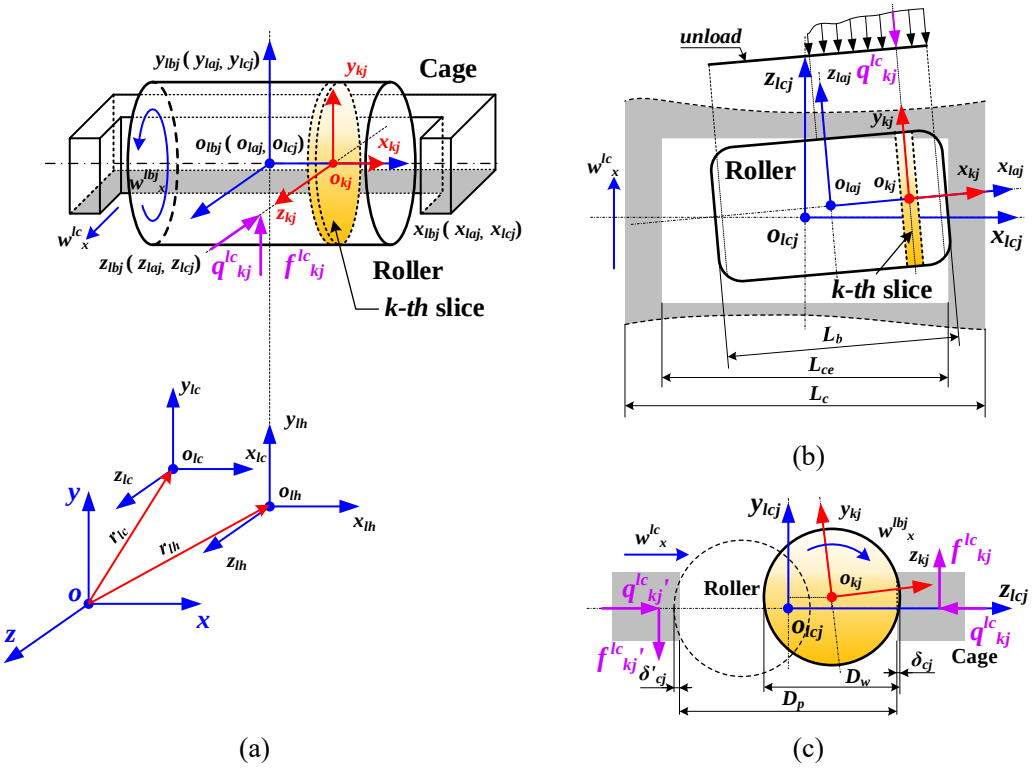

Fig. 5. Interaction between the cage pocket and roller based on the slicing method: (a) spatial geometry relationship; (b) stress distribution on pocket; (c) force analysis on k-th slice.

As shown in **Fig. 5(c)**, the interference between the pocket wall and the k-th slice on the roller is further obtained as follows:

$$\delta_{kj}^{lcj}=\left\{\left[\left(y_{kj}^{lcj2}+z_{kj}^{lcj2}\right)^{0.5}-c_k\right]-\left(D_p-D_w\right)/2 \quad 0\right\}_{\max} \tag{13}$$

where D_p denotes the pocket diameter.

Similar to the contact at the roller/raceway interface, the normal load between this slice and the pocket is further derived from Hertz's theory:

$$q_{kj}^{lc}=\frac{L_bE_1E_2}{1.319\cdot nL_{be}^{0.11}\left[E_2\left(1-v_1^2\right)+E_1\left(1-v_2^2\right)\right]}\cdot\delta_{kj}^{lcj1.11}\cdot sign\left(z_{kj}^{lcj}\right) \tag{14}$$

Since there is less lubricant in the roller/pocket gap, the friction between the two can be inferred from Coulomb friction:

$$f_{kj}^{lc}=-\mu_{ck}\cdot q_{kj}^{lc}\cdot sign\left(w_x^{lbj}\right) \tag{15}$$

where μ_{ck} is the Coulomb coefficient of friction between the cage and the roller, varying in time. Its

exact value is determined by the relative sliding velocity between the two contacting objects. The force vector exerted on the cage from the j-th roller can be further derived as:

$$F_{lcj}^{lbj} = \begin{bmatrix} [T_{lc}]^{-1} & 0 \\ 0 & [T_{lc}]^{-1} \end{bmatrix} \begin{bmatrix} [T_{lcj}^{lc}]^{-1} & 0 \\ 0 & [T_{lcj}^{lc}]^{-1} \end{bmatrix} \begin{bmatrix} 0 \\ -\sum_{k=1}^{n} f_{kj}^{lc} \\ \sum_{k=1}^{n} q_{kj}^{lc} \\ \sum_{k=1}^{n} f_{kj}^{lc} \cdot D_w/2 \\ -\sum_{k=1}^{n} q_{kj}^{lc} \cdot x_{kj} \\ -\sum_{k=1}^{n} f_{kj}^{lc} \cdot x_{kj} \end{bmatrix} \tag{16}$$

The interaction between the cage and the guiding ring is displayed in **Fig. 6**. Unlike random collision between the roller and pocket, once the cage reaches a steady state of operation, a hydrodynamic film forms between it and the guiding ring. Inevitably, however, the cage is occasionally subjected to external excitation, which can disrupt this hydrodynamic force and lead to direct contact between the two. Therefore, both of these possible scenarios need to be considered in the model. In either model, some parameters between them need to be specified first, such as the gap, velocity, and so on.

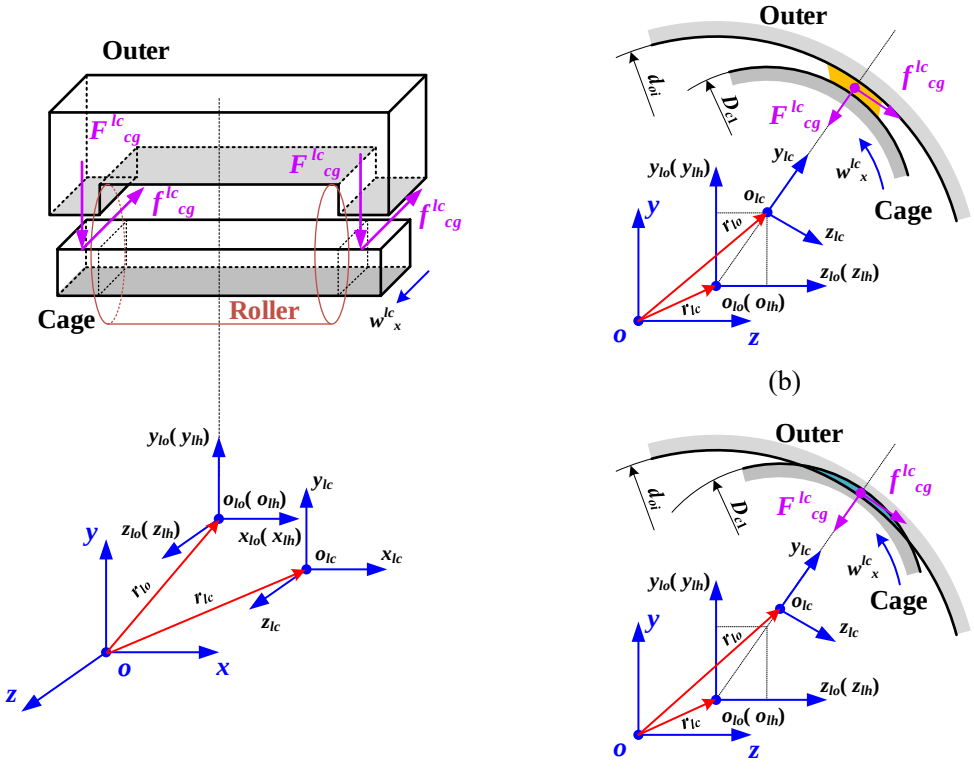

Fig. 6. Interaction between the cage and guiding ring: (a) spatial geometry relationship; (b)

hydrodynamic interaction; (c) dry contact.

As shown in **Fig. 6(a)**, the position vector of the cage center in the outer ring coordinate frame can be expressed as:

$$r_{lc}^{lo} = \left[T_{lo}\right]^{-1}\left(r_{lc} - r_{lo}\right) \tag{17}$$

where T_{lo} is the transformation matrix from the inertial coordinate frame to the outer coordinate frame.

The clearness or interference between the cage surface and the guiding surface is then obtained as follows:

$$\delta_{lc}^{lo} = \left(d_{oi} - D_{c1}\right)/2 - \left(y_{lc}^{lo2} + z_{lc}^{lo2}\right)^{0.5} \tag{18}$$

where d_{oi} is the diameter of the guiding surface, and D_{c1} is the cage outer surface diameter.

If there is a gap between the two surfaces ($\delta^{lo}_{lc} > 0$), it is assumed to be filled with lubricant. A steady fluid pressure is formed between them, which can be obtained from the theory of short journal bearings [53]:

$$F_{cg}^{lc} = \frac{\eta_0 u_{lc}^{lo} L_c^3 \delta_{lc}^{lo2}}{0.25\left(d_{oi} - D_{c1}\right)^2\left[1 - \delta_{lc}^{lo2}\right]^2} \tag{19}$$

$$f_{cg}^{lc} = \frac{\pi\eta_0 u_{lc}^{lo} L_c^3 \delta_{lc}^{lo2}}{\left(d_{oi} - D_{c1}\right)^2\left[1 - \delta_{lc}^{lo2}\right]^{1.5}} \cdot sign\left(v_{lc}^{lo}\right) \tag{20}$$

where η_0 is the viscosity of the lubricant, u^{lo}_{lc} and v^{lo}_{lc} are the rolling and sliding velocities between them, L_c is the cage width.

In some cases, such as external excitation, random excitation during the start-up phase, etc., interference between the cage surface and the outer guide surface may occurs ($\delta^{lo}_{lc} < 0$). The force formed between the two surfaces can be predicted by using Hertz's theory and Coulomb's law.

$$F_{cg}^{lc} = \frac{E_1 E_2 L_c^{9/8}}{4\left[E_2\left(1 - v_1^2\right) + E_1\left(1 - v_2^2\right)\right]} \cdot \left(\frac{-\delta_{lc}^{lo}}{0.39}\right)^{1.11} \tag{21}$$

$$f_{cg}^{lc} = -\mu_{cg} \cdot F_{cg}^{lc} \cdot sign\left(v_{lc}^{lo}\right) \tag{22}$$

where μ_{ck} is the Coulomb coefficient of friction between the two surfaces, varying in time.

The force vector exerted on the cage from the guiding ring can be further derived as:

$$F_{lc}^{lo} = \begin{bmatrix} \left[T_{lo}\right]^{-1} & 0 \\ 0 & \left[T_{lo}\right]^{-1} \end{bmatrix} \begin{bmatrix} \left[T_{lc}^{lo}\right]^{-1} & 0 \\ 0 & \left[T_{lc}^{lo}\right]^{-1} \end{bmatrix} \begin{bmatrix} 0 \\ -F_{cg}^{cl} \\ -f_{cg}^{cl} \\ -F_{cg}^{cl} \cdot D_{c1}/2 \\ 0 \\ 0 \end{bmatrix} \tag{23}$$

where T^{lo}_{lc} is the transformation matrix from the outer coordinate frame to the j-th pocket coordinate frame.

2.2.4 Differential equations for CRB components

Since each component within the bearings is considered a rigid body, the Newton-Euler law can be used to determine their motion in space.

$$\begin{bmatrix} m\ddot{x} \\ m\ddot{y} \\ m\ddot{z} \\ I_x\dot{w}_x - \left(I_y - I_z\right)w_y w_z \\ I_y\dot{w}_y - \left(I_z - I_x\right)w_z w_x \\ I_z\dot{w}_z - \left(I_x - I_y\right)w_x w_y \end{bmatrix} = F_{external} \tag{24}$$

where m is the mass, I is the moment of inertia, $\ddot{x}$ is the linear acceleration, $\dot{w}$ is the angular acceleration, and w is the angular speed. $F_{external}$ is the force vector exerted on the component.

It is worth noting that all displacement vectors, velocity vectors and acceleration vectors in this system of equations are obtained in the inertial coordinate frame. Since the loads and motions of the roller and cage are the most complex and critical components of CRB, they are discussed in detail in this part. **Figure 7** presents the forces exerted on them from other components.

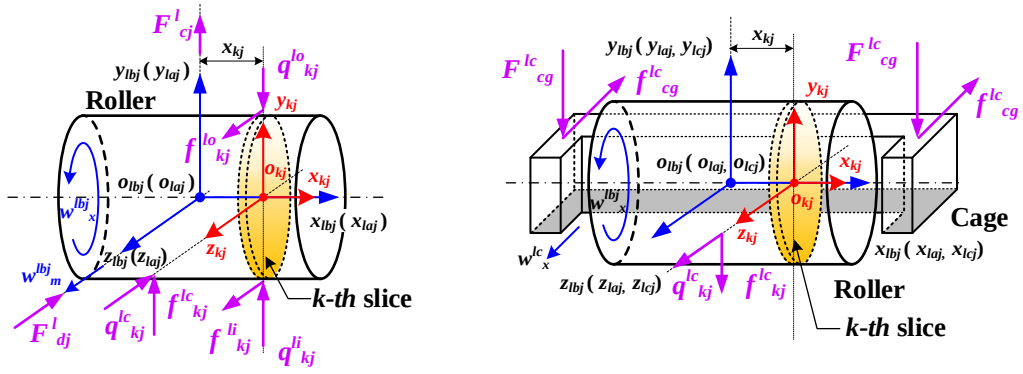

(a) (b)

Fig. 7. Schematic of the load vector exerted on CRB components: (a) loads exerted on the *j*-th roller; (b) loads exerted on the cage.

As shown in **Fig.7(a)**, the force vector exerted on the *j*-th roller from other components can be expressed as:

$$F_{external}^{lbj} = F_{bj}^{lr} + \begin{bmatrix} \left[T_{lbj}\right]^{-1} & 0 \\ 0 & \left[T_{lbj}\right]^{-1} \end{bmatrix} \begin{bmatrix} \left[T_{laj}^{lbj}\right]^{-1} & 0 \\ 0 & \left[T_{laj}^{lbj}\right]^{-1} \end{bmatrix} \begin{bmatrix} 0 & +0 \\ F_{cj}^{l} & +\sum_{k=1}^{n} f_{kj}^{lc} \\ F_{dj}^{l} & -\sum_{k=1}^{n} q_{kj}^{lc} \\ 0 & -\sum_{k=1}^{n} f_{kj}^{lc} \cdot D_w/2 \\ 0 & +\sum_{k=1}^{n} q_{kj}^{lc} \cdot x_{kj} \\ 0 & +\sum_{k=1}^{n} f_{kj}^{lc} \cdot x_{kj} \end{bmatrix} \tag{25}$$

where F^{l}_{cj} is the centrifugal force, and F^{l}_{dj} is the disturbance resistance of the lubricant.

As shown in **Fig.7(b)**, the force vector exerted on the cage from other components can be expressed as:

$$F_{external}^{lc} = \sum_{j=1}^{Z} F_{lcj}^{lbj} + F_{lc}^{lo} \tag{26}$$

where Z is the roller number.

2.2.5 Model validation of CRB

A test rig for CRB cage speed has been constructed to validate the present dynamic model. The structure of this test system is detailed in **Fig. 8**. As shown in **Fig. 8(a)**, it consists of four parts: drive motor, support shaft system, test bearing and data acquisition system. The drive speed and external load of the test CBR are provided by the drive motor and loading equipment. During the test, the reflective strip is fixed to one side of the CRB cage, and the acquisition system receives signals for each revolution. In addition, as shown in **Fig. 8(b)**, NU215 is selected as the test bearing, and its specific structural parameters are listed in **Table 1**.

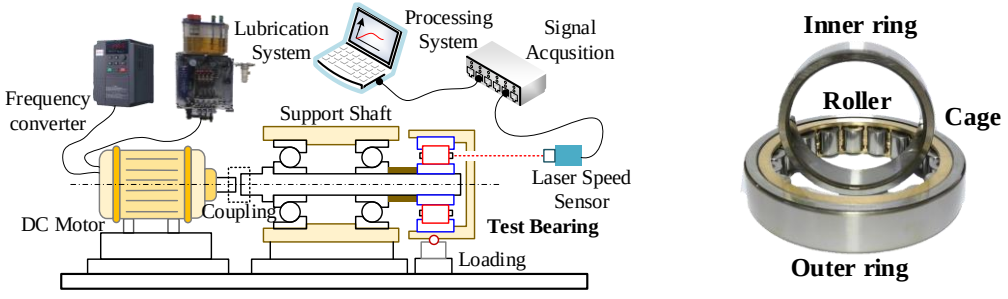

(a) (b)

Fig. 8. Schematic diagram of test rig for CRB cage speed: (a) Structure schematic diagram; (b) test bearing.

Table 1. List of main structural parameters for NU215

CRB component name	Structure parameter name	Value

Inner ring	Diameter of raceway d_i /mm	88.5
	Width B_i /mm	25
Outer ring	Diameter of raceway d_o /mm	118.57
	Width B_o /mm	25
Roller	Diameter D_w /mm	15
	Number Z	18
	Width L_b /mm	17
	Width without profiling L_{be} /mm	15.5
Cage	Diameter of Outer face D_{c1} /mm	113.5
	Width L_c /mm	24.2
	Diameter of pocket D_p /mm	16.4
	Width of pocket L_{ce} /mm	17.3

During the test, the drive speed of the test bearing was kept at 2400 r·min^{-1}and 3600 r·min^{-1}, respectively, and the radial load was gradually increased from 500 N to 3000 N. The change curves of the cage speed with radial load under different drive speeds were further obtained, as shown in **Fig. 9**. The results show that the error between the model predictions and the experimental test values is less than 15%, which proves that the model is reliable. The deviation between the two remains around 5% when the radial load is greater than 1500N. In the bearing-rotor system, the radial load applied to CRB is greater than this critical value. Therefore, the present model can be fully added to the bearing-rotor system model as a bearing constraint function.

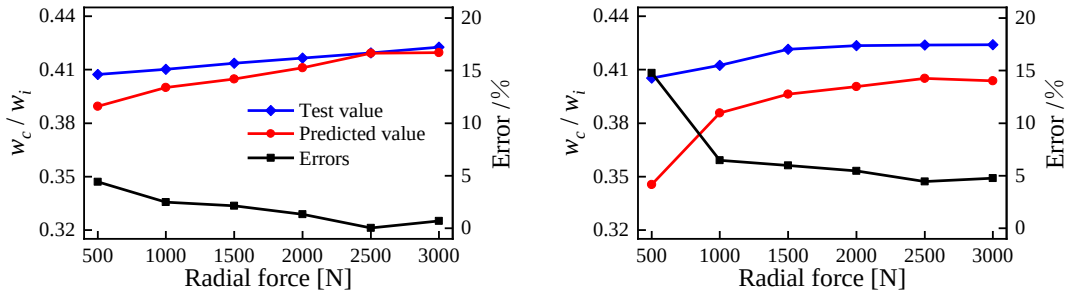

Fig. 9. Comparison between the experimental speed and the current model speed: (a) 2400 r·min^{-1}; (b) 3600 r·min^{-1}.

2.3 Dynamic modeling of rotor

The rotor flexibility is considered by defining the interactions between its discrete SFBEs. Therefore, the modeling of these interactions is discussed in detail in this Section. The schematic diagram of the interaction between neighboring SFBEs in the discrete rotor is presented in **Fig. 10**. Since the entire mass of each SFBE is considered to concentrate at its mass center, their motion can be determined by Newton-Euler law. Importantly, the SFBE at the rotor edges are subject to different constraints than those located inside it and therefore needs to be discussed separately.

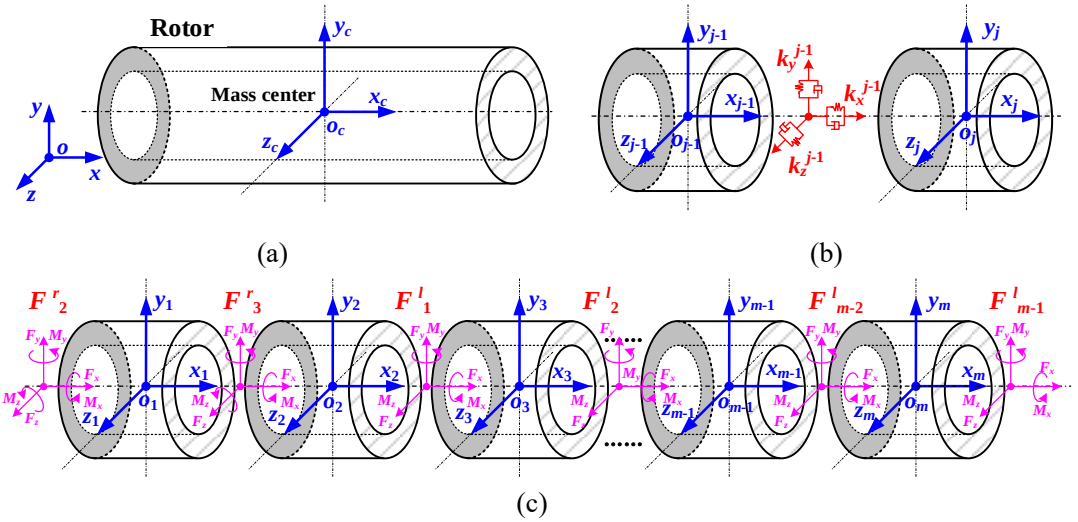

Fig. 10. Schematic diagram for the rotor flexibility between adjacent SFBEs: (a) rigid rotor; (b) definition of interaction; (c) discretized rotor.

Firstly, for an SFBE located at the left or right edge of the rotor, the motion is governed by the following equations:

$$\begin{bmatrix} m_{1(m)}\ddot{x}_{1(m)} \\ m_{1(m)}\ddot{y}_{1(m)} \\ m_{1(m)}\ddot{z}_{1(m)} \end{bmatrix} = \left[T_{1(m)}\right]^{-1} \begin{bmatrix} F^{r(l)}_{2(m-1)x} + F_{1(m)ex} + F_{1(m)cx} \\ F^{r(l)}_{2(m-1)y} + F_{1(m)ey} + F_{1(m)cy} + G_{1(m)} \\ F^{r(l)}_{2(m-1)z} + F_{1(m)ez} + F_{1(m)cz} \end{bmatrix} \tag{27}$$

$$\begin{bmatrix} I_{1(m)x}\dot{w}_{1(m)x} - \left(I_{1(m)y} - I_{1(m)z}\right)w_{1(m)y}w_{1(m)z} \\ I_{1(m)y}\dot{w}_{1(m)y} - \left(I_{1(m)z} - I_{1(m)x}\right)w_{1(m)z}w_{1(m)x} \\ I_{1(m)z}\dot{w}_{1(m)z} - \left(I_{1(m)x} - I_{1(m)y}\right)w_{1(m)x}w_{1(m)y} \end{bmatrix} = \begin{bmatrix} M^{r(l)}_{2(m-1)x} + M_{1(m)ex} \\ M^{r(l)}_{2(m-1)y} + M_{1(m)ey} \\ M^{r(l)}_{2(m-1)z} + M_{1(m)ez} \end{bmatrix} \tag{28}$$

where $T_{1(m)}$ is the transformation matrix from the inertial coordinate frame to the 1(m)-th SFBE coordinate frame. F^r is the force vector exerted on the 1-th SFBE from the 2-th SFBE, and F^l is the force vector exerted on the m-th SFBE from the (m-1)-th SFBE, which have been discussed in Ref. [51]. F_e is the force vector acting on the SFBE from external components such as bearings and gears, and M_e is the moment vector. F_c is eccentric load vector due to the presence of eccentric SFBE. G is the gravitational force of the SFBE.

Secondly, the equations of motion for SFBEs located inside the rotor (for example, 2-th SFBE) are:

$$\begin{bmatrix} m_2\ddot{x}_2 \\ m_2\ddot{y}_2 \\ m_2\ddot{z}_2 \end{bmatrix} = \left[T_2\right]^{-1} \begin{bmatrix} F^l_{1x} + F_{2ex} + F_{2cx} + F^r_{3x} \\ F^l_{1y} + F_{2ey} + F_{2cy} + F^r_{3y} + G_2 \\ F^l_{1y} + F_{2ez} + F_{2cz} + F^r_{3z} \end{bmatrix} \tag{29}$$

$$\begin{bmatrix} I_{2x}\dot{w}_{2x}-\left(I_{2y}-I_{2z}\right)w_{2y}w_{2z} \\ I_{2y}\dot{w}_{2y}-\left(I_{2z}-I_{2x}\right)w_{2z}w_{2x} \\ I_{2z}\dot{w}_{2z}-\left(I_{2x}-I_{2y}\right)w_{2x}w_{2y} \end{bmatrix}=\begin{bmatrix} M_{1x}^{l}+M_{2ex}+M_{3x}^{r} \\ M_{1y}^{l}+M_{2ey}+M_{3x}^{r} \\ M_{1z}^{l}+M_{2ez}+M_{3x}^{r} \end{bmatrix} \tag{30}$$

3. Solution of Bearing-rotor model

After the dynamic models for FPCBB, CRB, and rotor have been proposed separately, it is necessary to sort out the relationship among them to complete the mutual coupling, which will be discussed in detail in this section. The solution process of the bearing-rotor model is presented in **Fig. 11** to describe it more clearly.

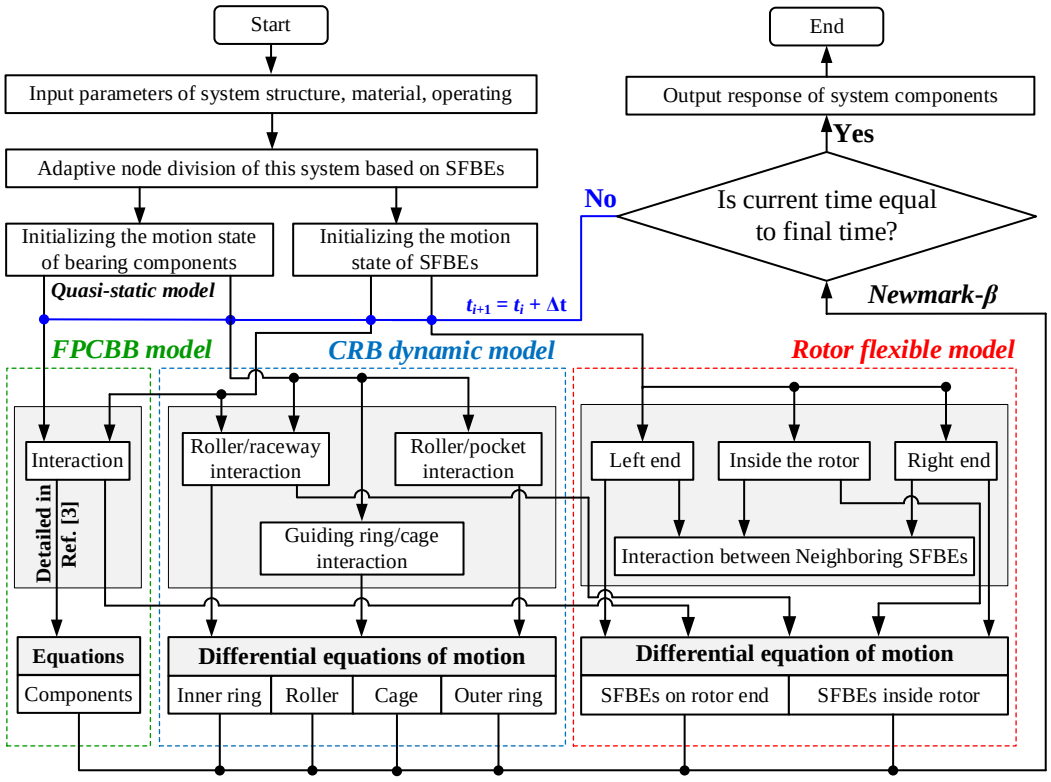

Fig. 11. Schematic diagram of solution process for the current bearing-rotor model

As shown in **Fig. 11**, all key parameters of the bearing-rotor system need to be input into these models firstly. The SFBE theory is used to discretize the system structure according to its specific structure. The motion state of the bearing components needs to be initialized by its quasi-static model to ensure the solution accuracy. With the help of the CRB, FPCBB [3], and rotor models, the motion state are converted to interactions between these components, which are further introduced into the differential equations. Newmark-β is used to solve these equations to obtain the motion state of these components at the current instant of time. If the set has not yet been reached, this state is used as the initial solution for the next moment and a new iteration is performed. Otherwise, the dynamic response of system component in the time domain is entered. In this process, the bearing

model converts the motion constraints into force vector, which in turn applied to the SFBE on the rotor.

4. Comparation between the rigid and flexible model

In this section, the key parameters of the input shaft in offshore wind gearbox, which is the most prone to failure in a gearbox, are entered into the bearing-rotor model as an example. Its dynamic performance is further derived after the solution process in Section 3. Finally, the effect of rotor flexibility on the system dynamic response is investigated.

4.1 Determination of system parameters

The system parameters include two categories: structural parameters and operating conditions. In terms of structure, they consist of the structural parameters of CRB, FPCBB, and rotor. Among these components, NU215 is selected as CRB and QJ215 as FPCBB, whose structural parameters can be obtained in Section 2.2 of [3]. Therefore, the structural parameters of the rotor are presented in this Section. The structural diagram of the rotor is further illustrated in **Fig. 12**, where the dimensional parameters of main structure are labeled.

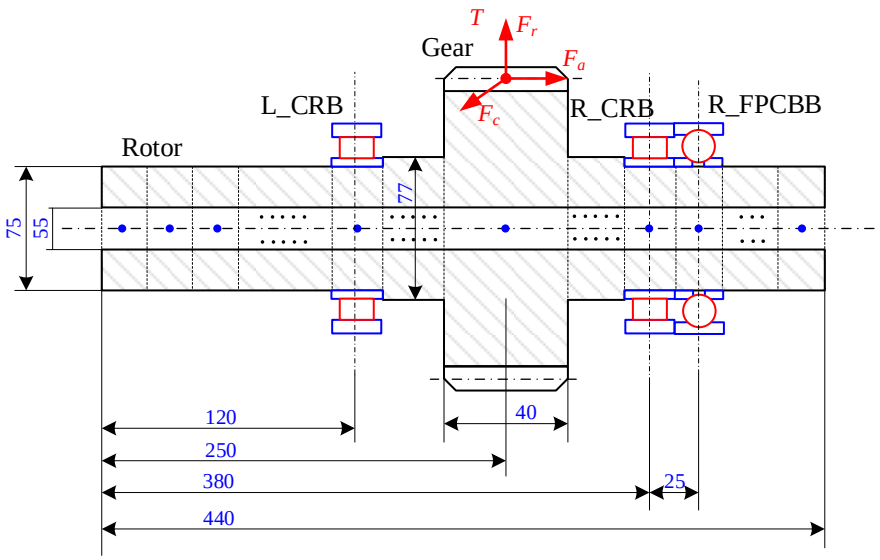

Fig. 12. Schematic diagram of key structural parameters for input shaft

According to the rotor structure shown in **Fig. 12**, the critical nodal information after discretization using SFBE theory are listed in **Table 2**. The bearings are located at nodes 11, 43 and 44. The external load is transmitted by the gear and is therefore applied at node 27.

Table 2. List of key structural parameters for input shaft

Number	Position /mm	Length * number /mm	Diameter /mm
1	0	10.75*10	75
	107.5	25*1 (L_CRB)	

	132.5		
		9.5*15	77
2	230		
		40*1	100
3	270		
		9.5*15	77
4	367.5		
		25*1 (R_CRB)	
	392.5		
		25*1 (R_FPCBB)	75
5	418.5		
		11.25*2	
	440		

The input operating conditions for offshore wind gearbox were used as the system service conditions [54], listed in **Table 3**.

Table 3. List of working condition parameters for input shaft in offshore wind gearbox

Drive speed / r·min^{-1}	Torque / N·m	External load /N		
		Circumferential (F_c)	Axial (F_a)	Radial (F_r)
3875	1000	9523.8	3094.5	3644.8
	1500	14286.0	4641.7	5467.2
	2000	19048.0	6188.9	7289.5

The information in **Table 2** was used to discretize the whole system to obtain its dynamic model, while its input operating conditions were provided by the data in **Table 3**. The system parameters are thus determined.

4.2 Comparation of prediction results

The rotor is first considered as a rigid body and therefore a rigid rotor model is proposed. Then, the node information in **Table 2** is used to discretize the rotor and construct a flexible rotor model. The effect of rotor flexibility on the dynamic behavior of the system is investigated by comparing the prediction results of the two models.

For avoiding the influence of bearing clearance on the predictions, the bearing clearance was determined to be 0.4 mm for CRB and 0.7 mm for FPCBB. Additionally, the dynamic behavior of the system mainly consists of the displacement of the nodes on the rotor and the load inside the bearing.

The nodal displacements on the rotor under different torques are presented in **Fig. 13**. As shown in **Fig.13(a)**, the nodal displacements increase with the gradual increment in the transmitted torque. Additionally, the nodal displacements predicted by the flexible model have an inverted “U” shape, while the displacements predicted by the rigid model has a linear shape. It is because the displacement predicted by the flexible model incorporates the elastic deformation of the rotor. The spatial motion of these node for a torque of 1500N is displayed in **Fig. 13(b)** to further investigate

the dynamic behavior of the rotor predicted by both models. As can be seen from **Fig. 13(b)**, the node motion is not a circular motion around the system axis, but a reciprocal motion around a point. The predictions of the two models are consistent in this regard, which may be due to the heavier external load.

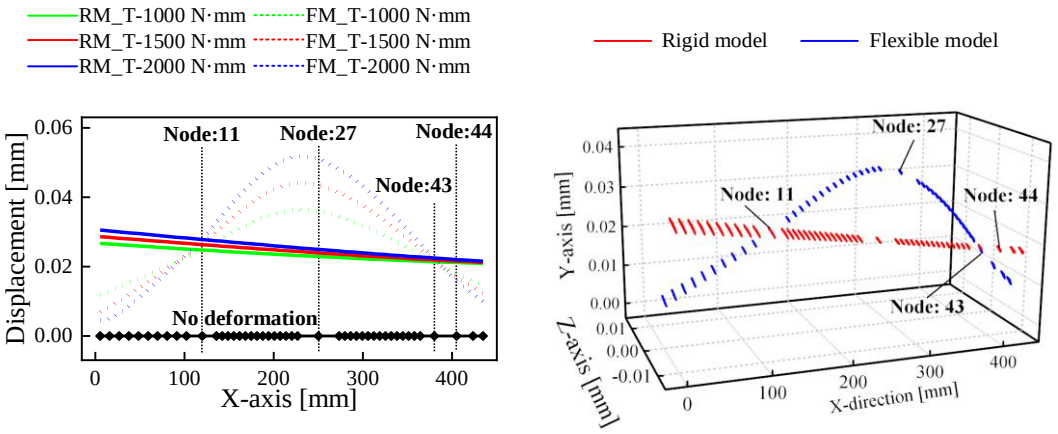

(a) (b)

Fig. 13. Effect of rotor flexibility on the node displacement under different torques: (a) nodal displacement; (b) T-1500 N·mm.

It can be seen from **Fig. 13** that the nodal displacements are strongly influenced by the bearing constraints. The inner ring orbits of the bearing in the radial plane for different torques are further presented in **Fig. 14**. For the left CRB (L_CRB), the effect of rotor flexibility on their orbits is almost negligible. However, it has a significant effect on the inner ring orbits of FPCBB (R_FPCBB). As the transmitted torque increases, the orbits of both CRBs gradually move to the upper left. For FPCBB, the orbit of inner ring predicted by the rigid model is in the same direction as that of CRB, but the orbit predicted by the flexible model is in the opposite direction.

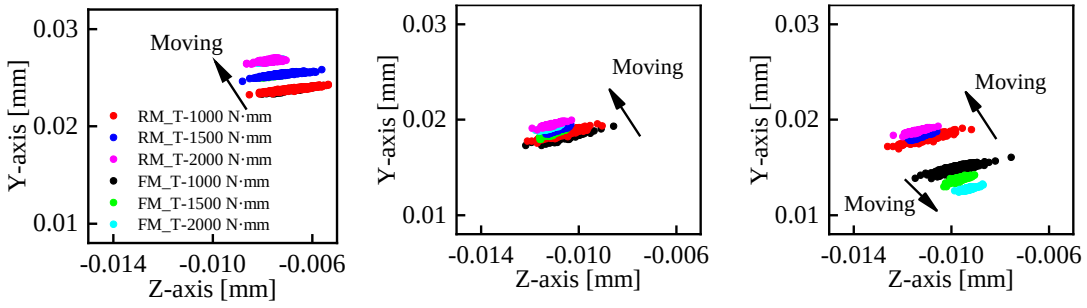

(a) (b) (c)

Fig. 14. Effect of rotor flexibility on the bearing displacement under different torques: (a) L_CRB; (b) R_CRB; (c) R_FPCBB.

The effect of rotor flexibility on the bearing dynamic behaviors cannot be fully reflected by the orbit of the bearing inner ring alone. It is necessary to further investigate it from the contact features at the rolling element/raceway interface. The contact features inside the left CRB (L_CRB) are firstly presented in **Fig. 15**. As shown in **Fig. 15(a)**, there is almost no significant difference in the

prediction of contact load between the two models. However, as shown in **Figs. 15(b)** and **(d)**, significant stress concentration in the inner raceway are predicted by the flexible model. The rigid model, on the other hand, performs poorly in this regard. It could potentially lead to incorrect estimation of bearing life. A similar phenomenon exists for the stress distribution in the outer raceway in **Figs. 15(c)** and **(e)**.

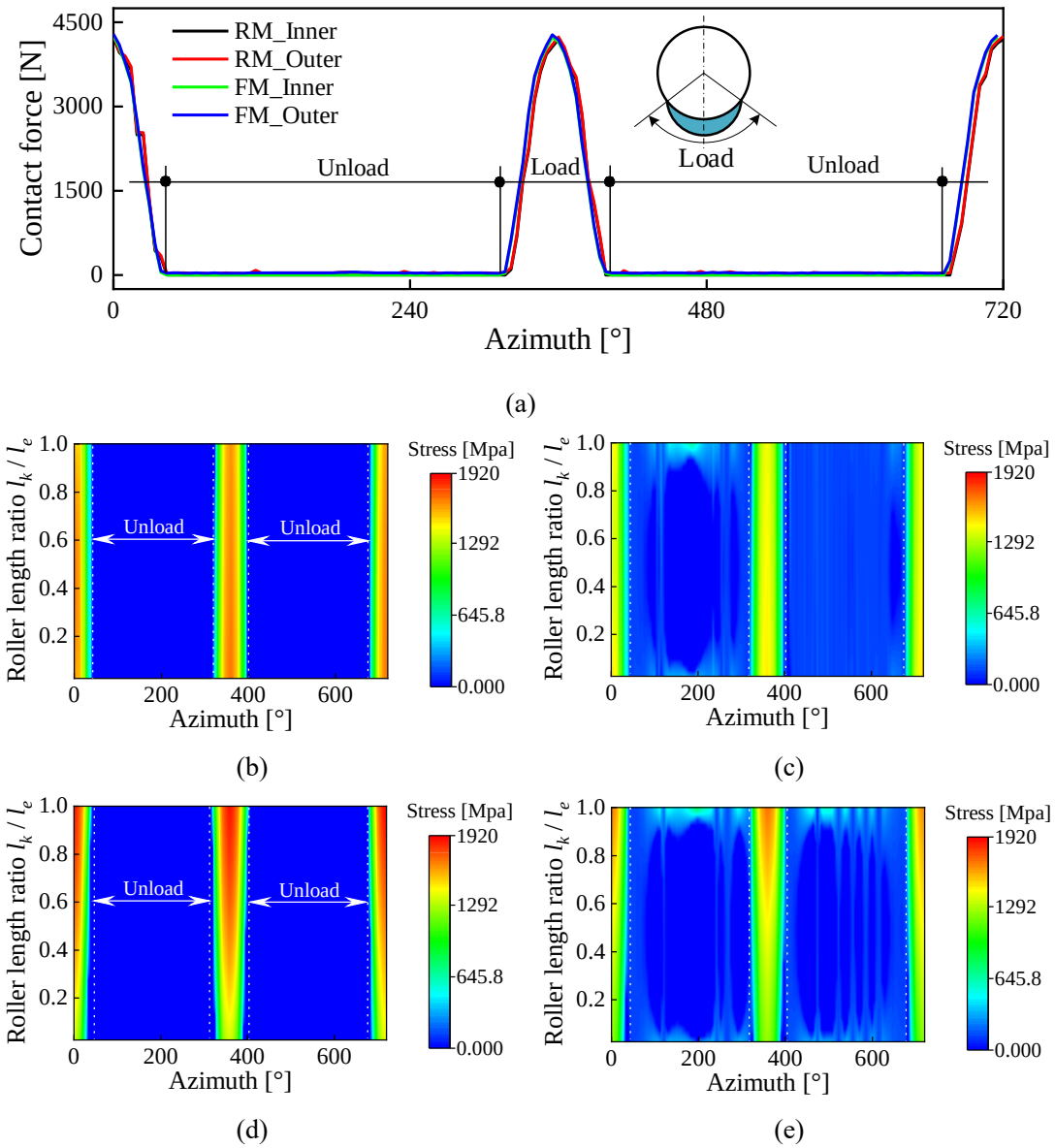

Fig. 15. Effect of rotor flexibility on contact feature inside L_CRB at 1500 N·mm: (a) load distribution inside L_CRB; (b) stress at inner raceway (RM); (c) stress at outer raceway (RM); (d) stress at inner raceway (FM); (e) stress at outer raceway (FM).

The effect of rotor flexibility on the contact feature inside the right CRB (R_CRB) is displayed in **Fig. 16**. **Fig. 16(a)** shows that the contact load predicted by the rigid model is heavier than that of the flexible model. This may due to the fact that the rotor deformation under external loads is sensed by the flexible model, and hence the load distributed on this bearing is slight. The stress aggregation predicted by the flexible model is still present as can be seen in **Figs. 16(b)**, **(c)**, **(d)**, and **(e)**.

Although a heavier contact load can be simulated by the rigid model, the maximum contact stress of the flexible model is greater than that of the rigid model duo to stress aggregation.

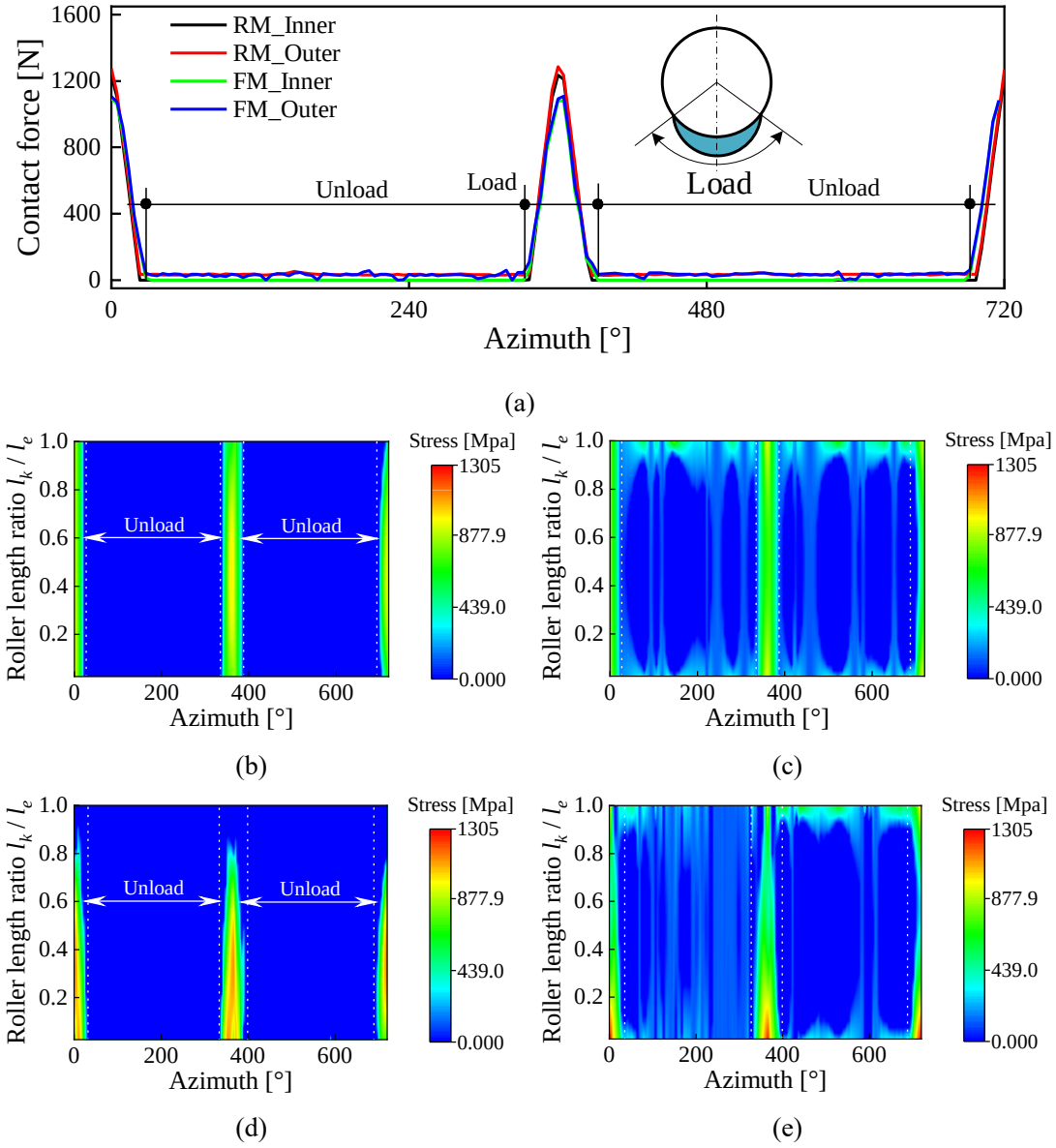

Fig. 16. Effect of rotor flexibility on contact feature inside R_CRB at 1500 N·mm; (a) load distribution inside R_CRB; (b) stress at inner raceway (RM); (c) stress at outer raceway (RM); (d) stress at inner raceway (FM); (e) stress at outer raceway (FM).

For the right FPCBB (R_FPCBB), the difference between the two model predictions is presented in **Fig. 17**. As shown in **Figs. 17(a)** and **(b)**, the difference between the contact loads predicted by the two models is not considerable. Notably, its multi-point contact state is only sensed by the flexible model. Once the bearing is in this state, the heat generation inside the bearing increases dramatically, leading to premature bearing failure. As can be seen in **Figs. 17(c)** and **(d)**, the two models differed significantly in predicting the contact angle on outer raceway, but not much in predicting the inner raceway contact angle.

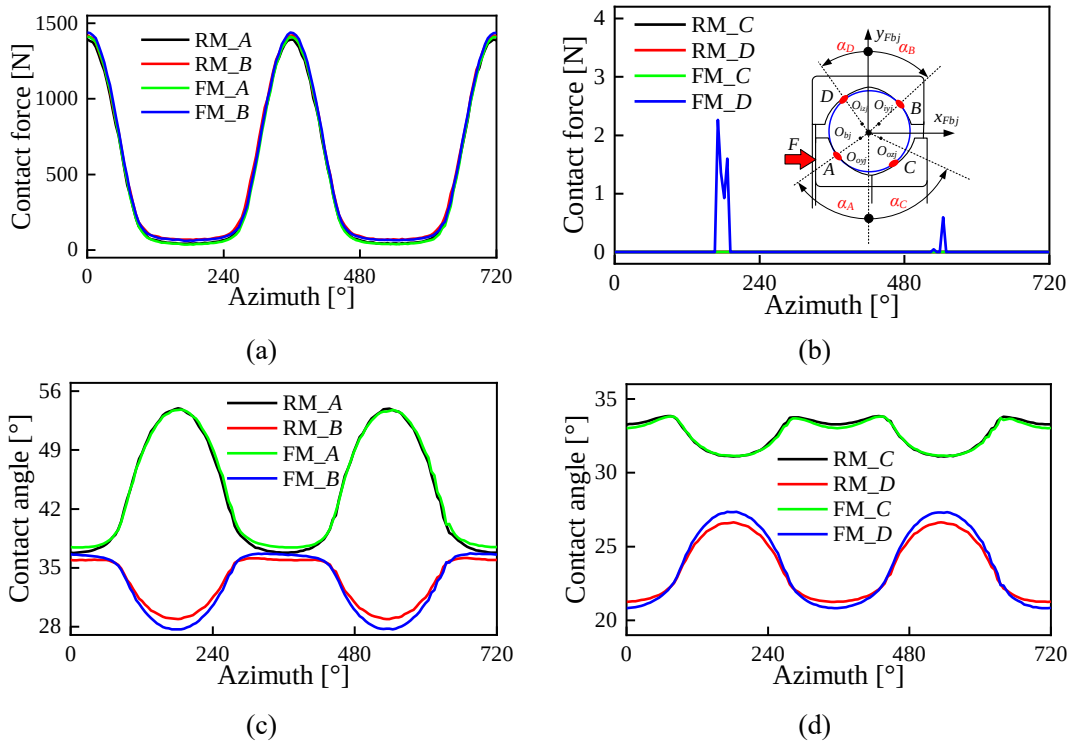

Fig. 17. Effect of rotor flexibility on contact feature inside R_FPCBB at 1500 N·mm: (a) load distribution at main-contact pair; (b) load distribution at sub-contact pair; (c) contact angle at main-contact pair; (d) contact angle at sub-contact pair.

In conclusion, compared with the rigid model, the flexible model is able to sense the elastic deformation of the rotor under external loads, and therefore its prediction results are closer to the actual operating state of the system. In addition, the system fatigue life predicted by the rigid model may deviate from the actual life due to the inability to sense the raceway's uneven wear.

5. Investigation on bearing clearance matching

Bearing clearances have a great influence on the dynamic behavior of the bearing-rotor system, especially the interaction among bearings with different clearances on the same rotor. Therefore, the effect of CRB and FPCBB clearances on the system performance is discussed in this Section, where a flexible rotor is considered. A drive speed of 3875 r·min^{-1} and a transmission torque of 1500 N·m have been applied to the input shaft of the gearbox. Nodal displacement of the rotor, contact features, sliding velocities and fatigue life of the bearing have been picked as performance indicators.

5.1 Effect of FPCBB clearance

Firstly, the effect of FPCBB with different clearances on the system performance is investigated. While the clearance of CRB is kept constant at 0.070 mm, the clearance of FPCBB is uniformly distributed between 0.030 mm and 0.110 mm. The variation of nodal displacement with FPCBB clearance is presented in **Fig. 18**. As shown in **Fig. 18(a)**, as the clearance increases, the nodes on the left side of L_RCB move closer to the system axis, while the nodes on its right side move away from the axis. To explore this issue further, the inner ring's motion of three bearings at different

clearances is given in **Figs. 18(b)**, **(c)** and **(d)**. Compared to the two bearings on the right (R_CRB and R_FPCBB), L_CRB motion is slightly affected by FPCBB clearance. The position change of the two bearings decreases as the clearance increases.

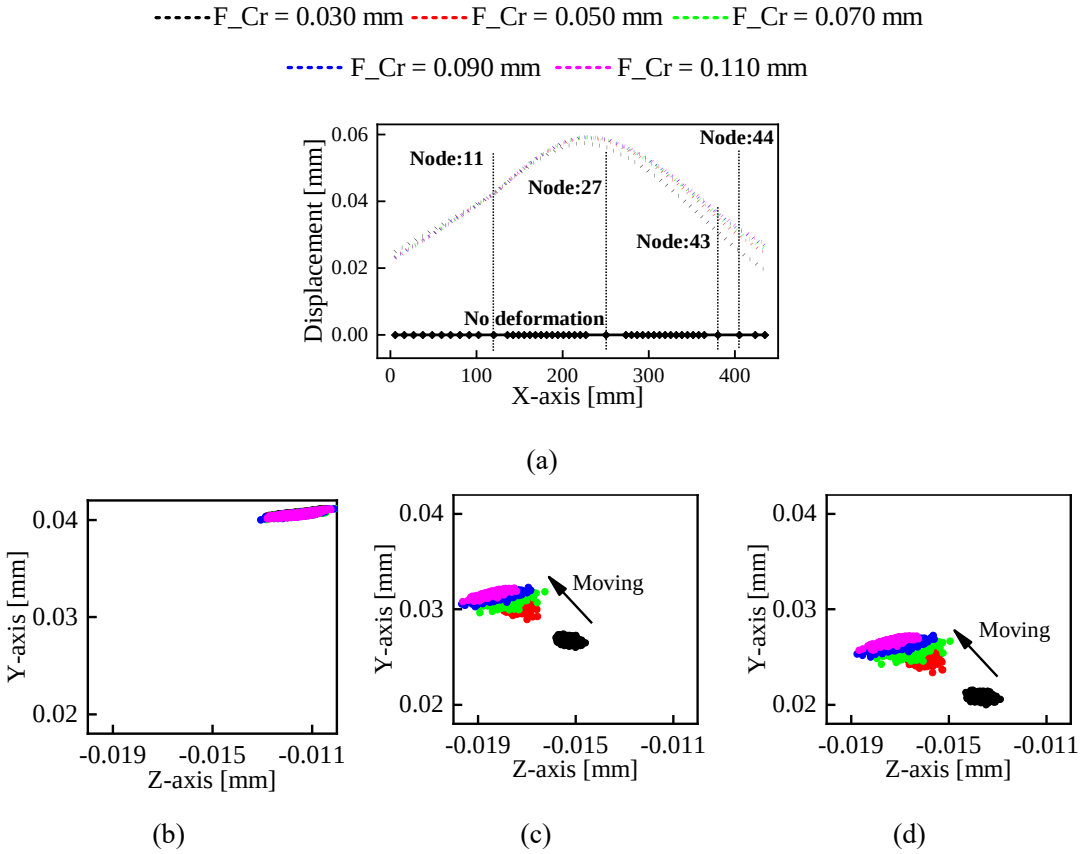

Fig. 18. Variation of node displacement with different FPCBB clearances: (a) nodal displacement; (b) L_CRB; (c) R_CRB; (d) R_FPCBB.

Variations in FPCBB clearance can change the displacement of the inner ring of these bearings, thus seriously affecting the contact characteristics inside them. Therefore, the effect of FPCBB clearance on the contact features of L_CRB is discussed first, as shown in **Fig. 19**. By observing **Figs. 19(a)** and **(b)**, it can be seen that the effect of the clearance on contact force of L_CRB is very slightly. This may be due to the poor ability of the ring displacement of this bearing to sense the change in FCPBB clearance. As for the contact stress at the inner raceway, as presented in **Figs. 19(c)** and **(d)**, its distribution along the roller generatrix seems to be influenced by FPCBB clearances. As the clearance increases, stress concentrations tend to occur on this raceway. A similar phenomenon is shown for the outer raceway in **Figs. 19(e)** and **(f)**. The stress concentration appears to be more pronounced.

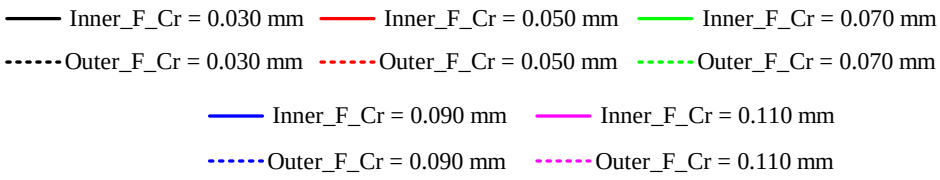

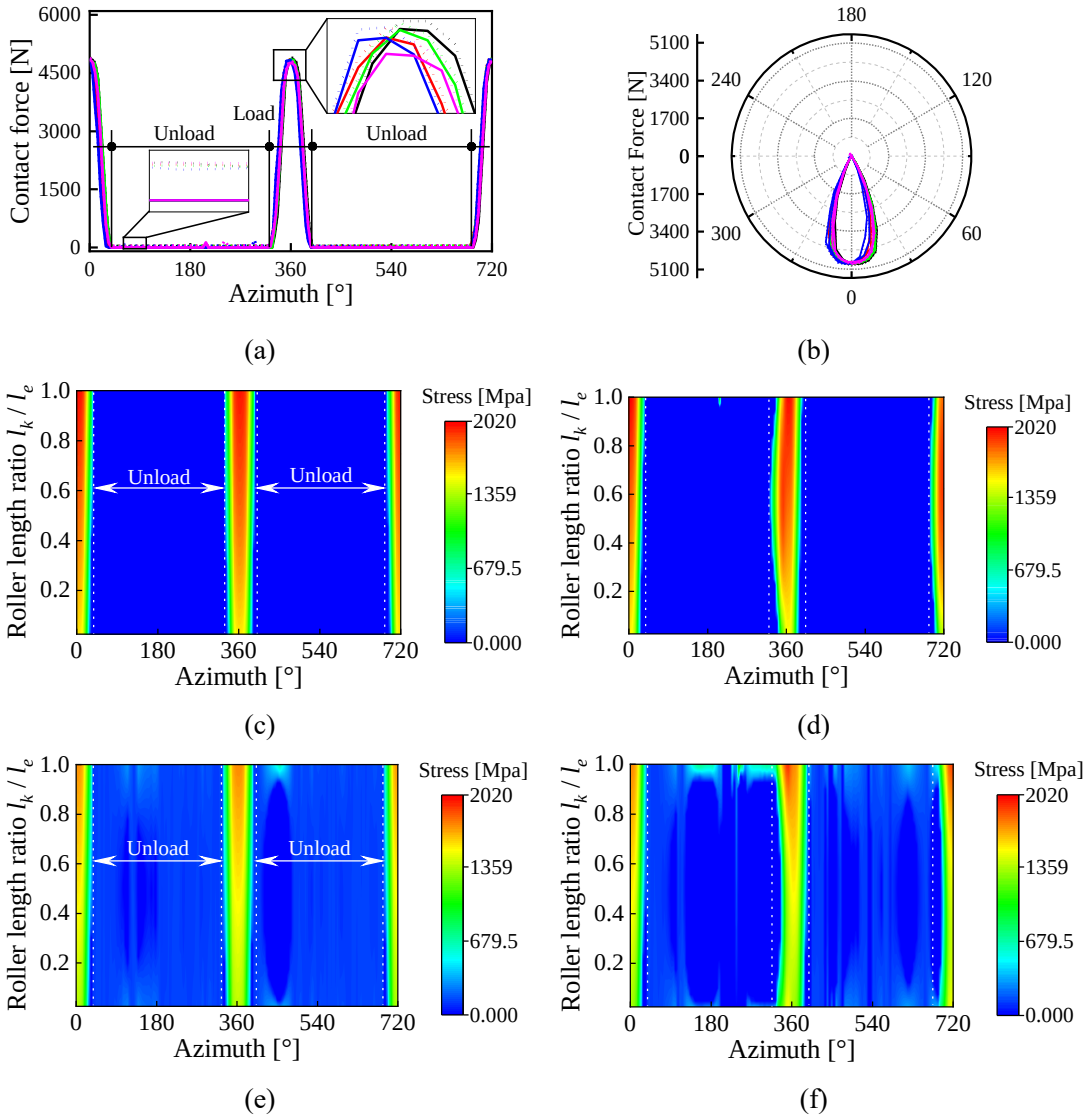

Fig. 19. Effect of FPCBB clearance on contact feature inside L_CRB: (a) contact load at different azimuths; (b) contact load radar diagram; (c) stress at inner raceway (F_Cr = 0.030); (d) stress at inner raceway (F_Cr = 0.110); (e) stress at outer raceway (F_Cr = 0.030); (f) stress at outer raceway (F_Cr = 0.110).

The contact features inside R_CRB under different FPCBB clearances is displayed in **Fig. 20**. From **Figs. 20(a)** and **(b)**, FPCBB clearance has a significant effect on the contact load inside L_CRB. As the clearance increases, the load applied to the roller becomes heavier. When FPCBB clearance is 0.030 mm, it takes almost all the load, resulting in no load on R_CRB. This is also illustrated in **Figs. 20(c)** and **(e)**, where there is no stress exerted on the roller at any azimuth. It means that there is significant sliding inside R_CRB, which affects the quality of the raceway surface. The stress distribution in the roller inside R_CRB for FPCBB clearance of 0.110 mm is presented in **Figs. 20(d)** and **(f)**. Although the sliding inside R_CRB is suppressed to some extent, there is an abnormal concentration of stress on the inner and outer raceways.

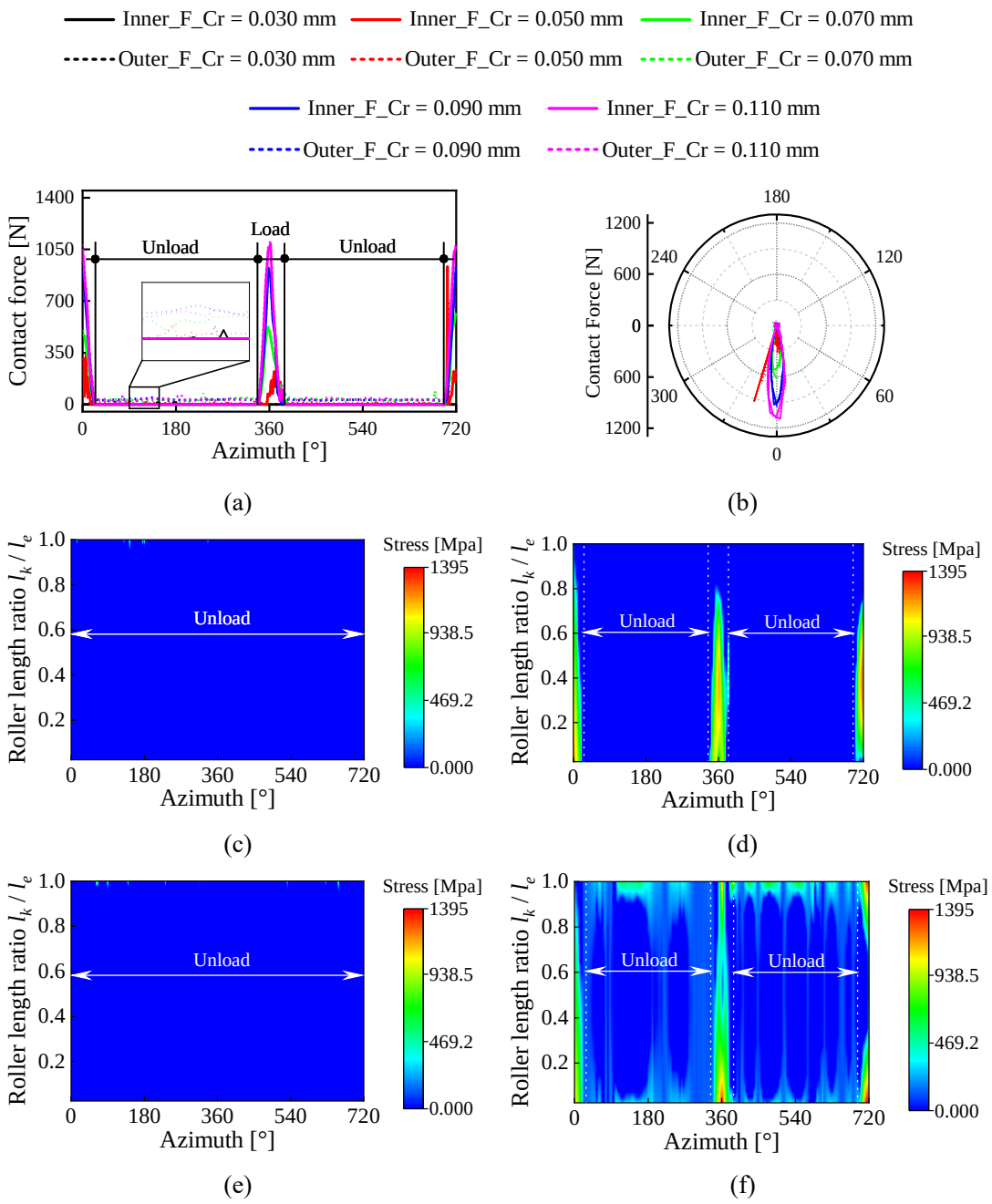

Fig. 20. Effect of FPCBB clearance on contact feature inside R_CRB: (a) contact load at different azimuths; (b) contact load radar diagram; (c) stress at inner raceway (F_Cr = 0.030); (d) stress at outer raceway (F_Cr = 0.110); (e) stress at outer raceway (F_Cr = 0.030); (f) stress at outer raceway (F_Cr = 0.110).

As for R_FPCBB, the effect of the clearance on its contact features is illustrated in **Fig. 21**. As shown in **Figs. 21(a)** and **(b)**, there is insignificant effect of the clearance on the load of the main-contact pair, while its influence on that of the sub-contact pair is abnormally pronounced. Variations in the clearance will result in changes in the contact state within FPCBB. For example, as the clearance increases, the ball will gradually move out of contact with the C-th raceway at certain azimuths. The smaller the clearance, the heavier the maximum contact load at the C-th raceway. From **Figs. 21(c)** and **(d)**, with increasing clearance, the contact angles of the sub-contact pair tend

to increase, while that of the sub-contact pair show the opposite trend. This indicates that the ball displacement is significantly shifted as the clearance changes.

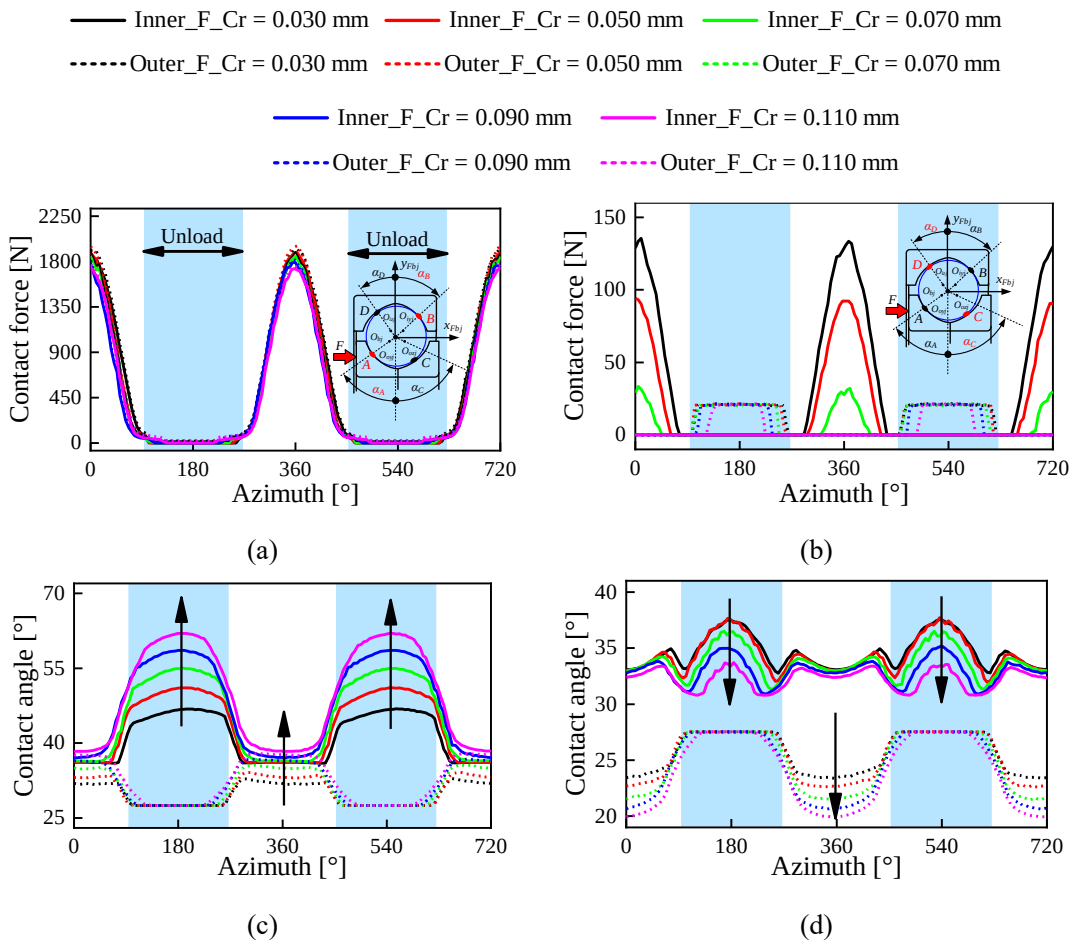

Fig. 21. Effect of FPCBB clearance on contact feature inside R_FPCBB: (a) load distribution at main-contact pair; (b) load distribution at sub-contact pair; (c) contact angle at main-contact pair; (d) contact angle at sub-contact pair.

Since the bearing dynamic performance cannot be determined exclusively by its contact features, it is necessary to investigate the effect of the clearance on its internal sliding. The speed characteristics of the three bearings for different clearances are presented in **Fig. 22**. As shown in **Figs. 22(a)** and **(b)**, the speed feature of the roller in L_CRB is not much affect by the clearance in the load zone. However, for R_CRB, as shown in **Figs. 22(c)** and **(d)**, as FPCBB clearance increases, the sliding on its raceway is greatly inhibited, thus significantly reducing the risk of failure. At a clearance of 0.030 mm, the roller inside R_CRB hardly move at all, resulting in severe scoring of the raceway surface. This is all due to an inappropriate choice of clearance, which results in the external loads applied to the bearing not being able to completely inhibit its internal sliding. **Figs. 22(e)** and **(f)** presents the variations of the speed features inside R_FPCBB with different clearances. The area with most severe sliding inside this bearing is the entrance to the load zone. The higher the selected clearance, the more serious the sliding. In some cases of clearance, the sliding velocity on the raceway can reach at 6 $m \cdot s^{-1}$. Therefore, the sliding inside the two right bearings should be taken into account when determining FCPBB clearance.

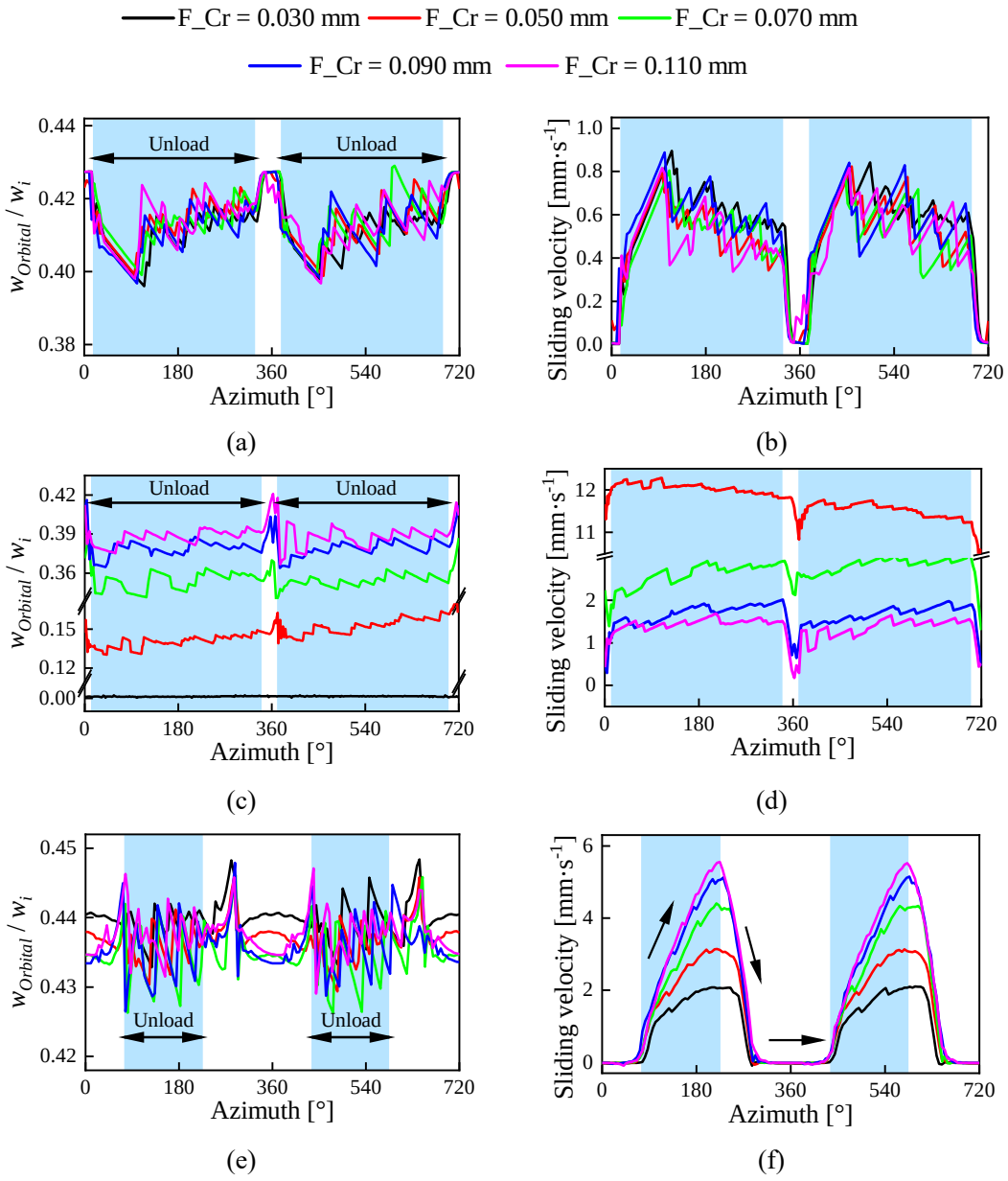

Fig. 22. Sliding features inside the bearing under different FPCBB clearances: (a) roller's orbital speed (L_CRB); (b) sliding velocity of raceway (L_CRB); (c) roller's orbital speed (R_CRB); (d) sliding velocity of raceway (R_CRB); (e) ball's orbital r speed (R_FPCBB); (f) sliding velocity of raceway (R_FPCBB).

The equivalent load and fatigue life of these three bearings at different clearances are further given in **Fig. 23**. As can be seen from **Figs. 23(a)** and **(b)**, the effect of FPCBB on these indicators of L_CRB is very slight, both in terms of load and life. **Figs. 23(c)** and **(d)** show that equivalent load exerted on R_CRB becomes heavier as the clearance increases. It means that the fatigue life of this bearing is considerably reduced. However, due to the significant sliding within the bearing, its fatigue life may increase with increasing clearance. As shown in **Figs. 23(e)** and **(f)**, with a gradual increment in clearance, the equivalent load applied to R_FPCBB is reduced. It is in contrast to the trend of contact load changes in some raceways. The reason for this is the introduction of new

contact points inside R_FPCBB, which reduces the probability of fatigue failure.

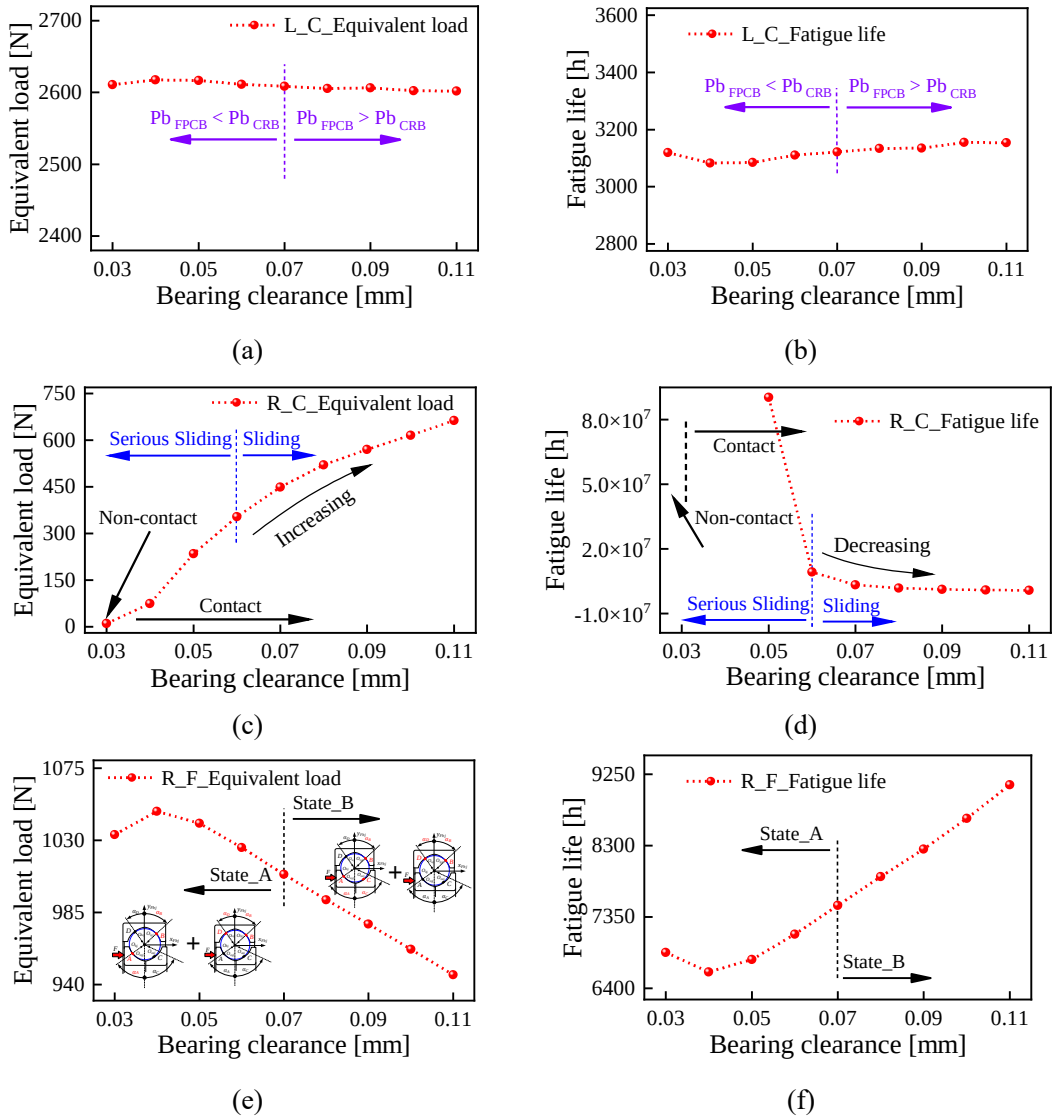

Fig. 23. Effect of FPCBB clearance on bearing fatigue life: (a) equivalent load (L_CRB); (b) fatigue life (L_CRB); (c) equivalent load (R_CRB); (d) fatigue life (R_CRB); (e) equivalent load (R_FPCBB); (f) fatigue life (R_FPCBB).

In summary, changes in FPCBB clearance have little effect on L_CRB. In contrast, both R_CEB and R_FPCBB are very sensitive to its changes. Considering the effect of raceway sliding on bearing fatigue life, the service life of both bearings in the right-hand side increases with growing FPCBB clearance. However, R_FPCBB has a high risk of raceway scuffing at the entrance of the load zone.

5.2 Effect of CRB clearance

The influence of CRB clearance on the dynamic behavior of the bearing-rotor system is then considered. The clearance of both CRB is picked up evenly between 0.030 mm and 0.110 mm, while the FPCBB clearance is fixed at 0.070 mm. Similar to FPCBB clearance, the investigation is concerned with the dynamic performance of rotor and bearings.

Fig. 24 presents the nodal displacements on the rotor for different CRB clearances. As shown in **Fig.**

24(a), the CRB clearance has much significant effect on its node displacement compared to FPCBB clearance. The displacement of each node on the rotor expands with the increment of CRB clearance. As shown in **Figs. 24(b)**, **(c)** and **(d)**, the effect of CRB clearance on the displacement of the three bearings is not uniform in intensity. For R_CRB and R_FPCBB, the rate of change in their displacements reduces considerably when the clearance exceeds a certain value. In contrast, the displacement of L_CRB maintains the same upward trend as the clearance increases.

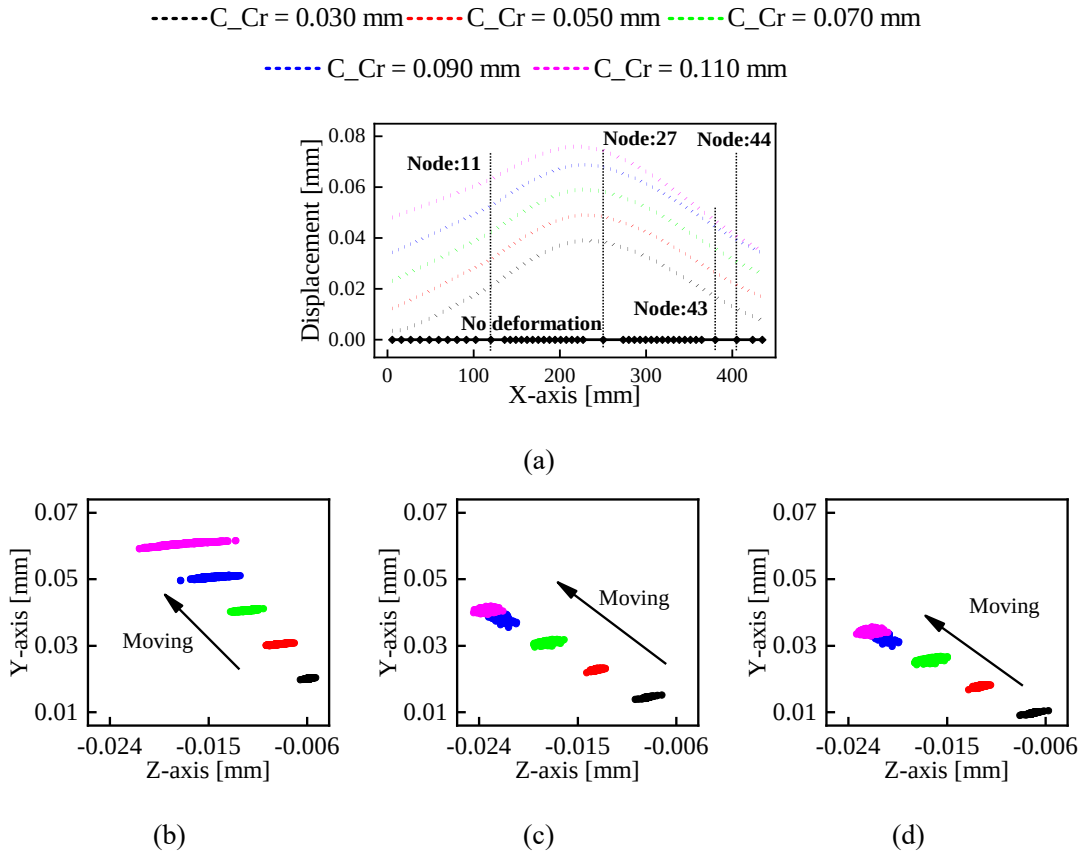

Fig. 24. Variation of node displacement with different CRB clearances: (a) nodal displacement; (b) L_CRB; (c) R_CRB; (d) R_FPCBB.

The contact characteristics of the roller inside L_CRB with different CRB clearances are presented in **Fig. 25**. As shown in **Figs. 25(a)** and **(b)**, the contact load on the roller becomes progressively heavier and the load area is reduced as the clearance increase. It has the potential to shorten the bearing fatigue life and lead to premature failure of the system. As can be seen in **Figs. 25(c)**, **(d)**, **(e)** and **(f)**, excessive clearance in CRB significantly increases the maximum stress on the contact interface between the roller and the two raceways, but also considerably reduces their stress concentration.

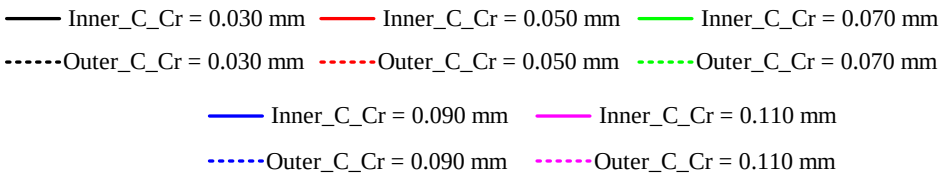

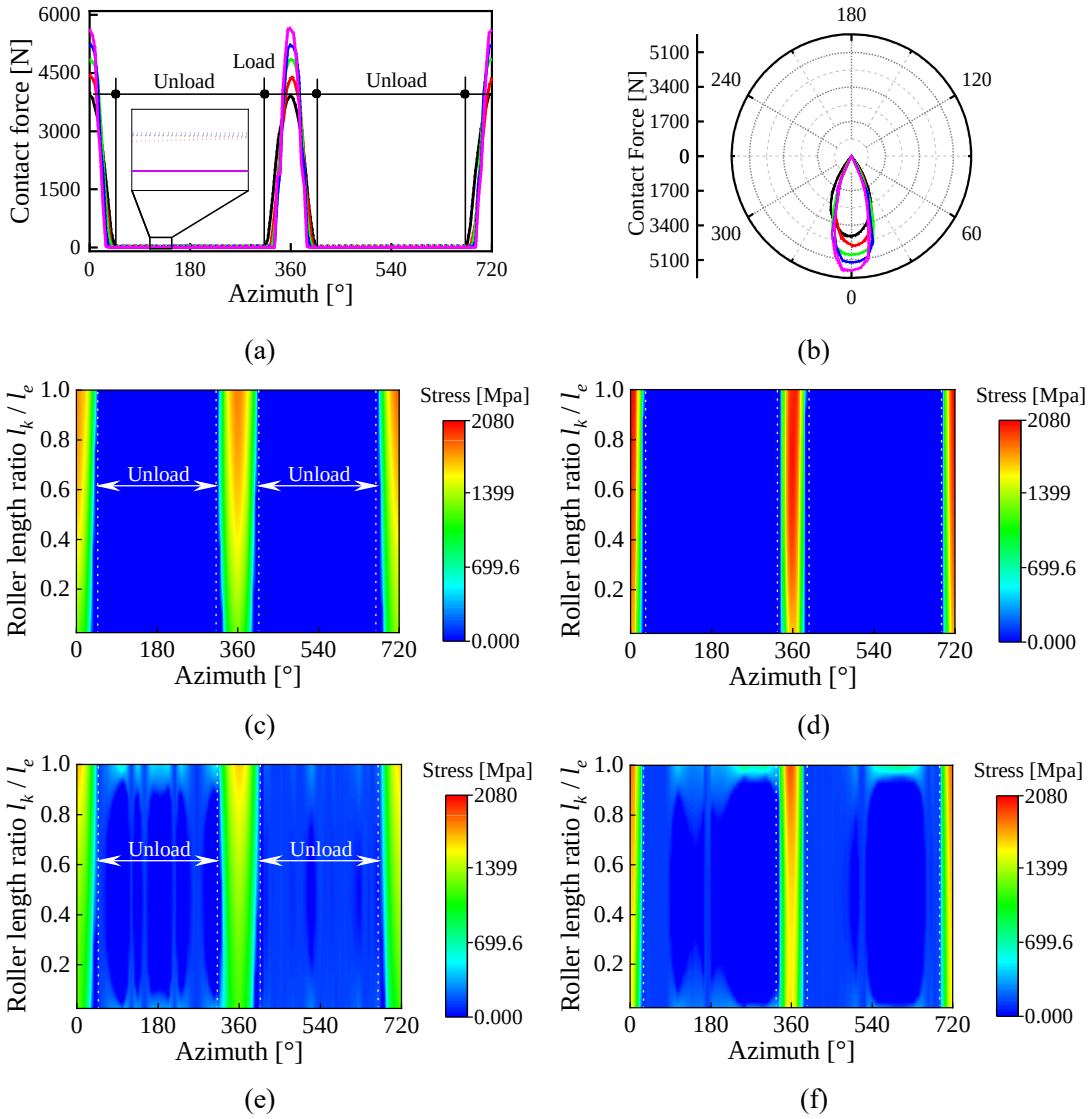

Fig. 25. Effect of CRB clearance on contact feature inside L_CRB: (a) contact load at different azimuths; (b) contact load radar diagram; (c) stress at inner raceway (C_Cr = 0.030); (d) stress at inner raceway (C_Cr = 0.110); (e) stress at outer raceway (C_Cr = 0.030); (f) stress at outer raceway (C_Cr = 0.110).

Figure 26 illustrates the variation of contact feature inside R_CRB with different CRB clearances. Excessive clearance can considerably reduce the contact load and load area inside this bearing, which can be seen in **Figs. 26(a)** and **(b)**. Once the clearance exceeds 0.070 mm, the external load applied to R_CRB is virtually non-existent, resulting in a loss of load on the roller. Bearing sliding can be very serious and lead to premature bearing failure, as discussed in detailed below. **Figs. 26(c)** and **(e)** show that there is a serious unevenness of wear on the both raceways with a clearance of 0.030 mm. As shown in **Figs. 26(d)** and **(f)**, when the clearance is 0.110 mm, there is no stress between the raceways and roller, which means that the bearing is not affected by external loads.

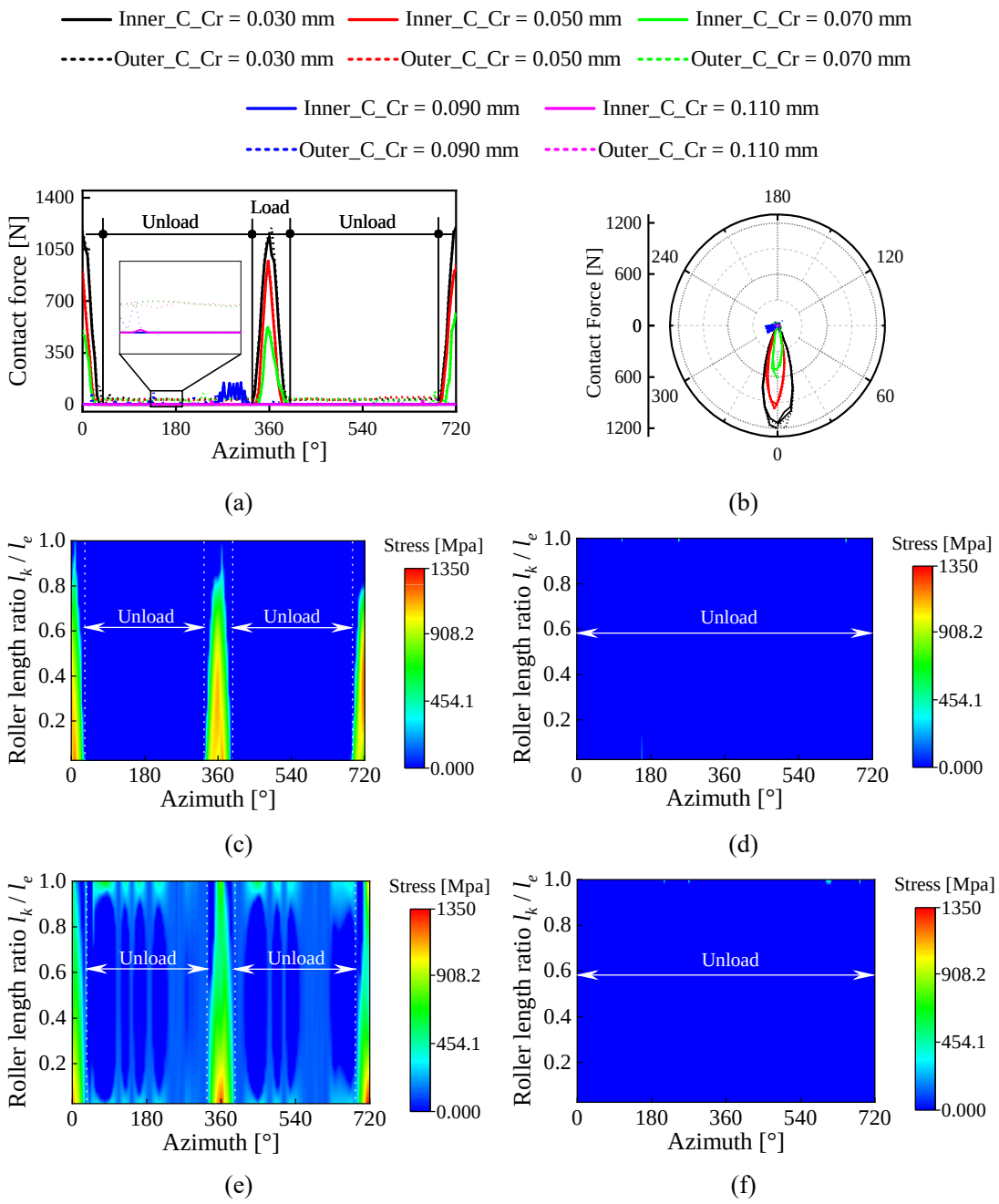

Fig. 26. Effect of CRB clearance on contact feature inside R_CRB: (a) contact load at different azimuths; (b) contact load radar diagram; (c) stress at inner raceway (C_Cr = 0.030); (d) stress at inner raceway (C_Cr = 0.110); (e) stress at outer raceway (C_Cr = 0.030); (f) stress at outer raceway (C_Cr = 0.110).

The effect of CRB clearance on contact feature inside R_FPCBB is presented in **Fig. 27**. As shown in **Figs. 27(a)** and **(b)**, as the clearance increases, the load distribution inside R_FPCBB becomes severely uneven and its load zone tends to shrink. The maximum load inside it becomes progressively heavier, which may lead to premature its fatigue failure. Furthermore, once the clearance is exceeding 0.030 mm, a third contact point begins to appear inside this bearing. In this case, the influence of the clearance on the contact angle of the main-contact pair is reduced, especially in the unloaded zone, as shown in **Fig. 27(c)**. As for the contact angle of the sub-contact

pair in **Fig. 27(d)**, the contact angle of the inner raceway is always greater than that of the outer raceway, and both are greatly affect by CRB clearance.

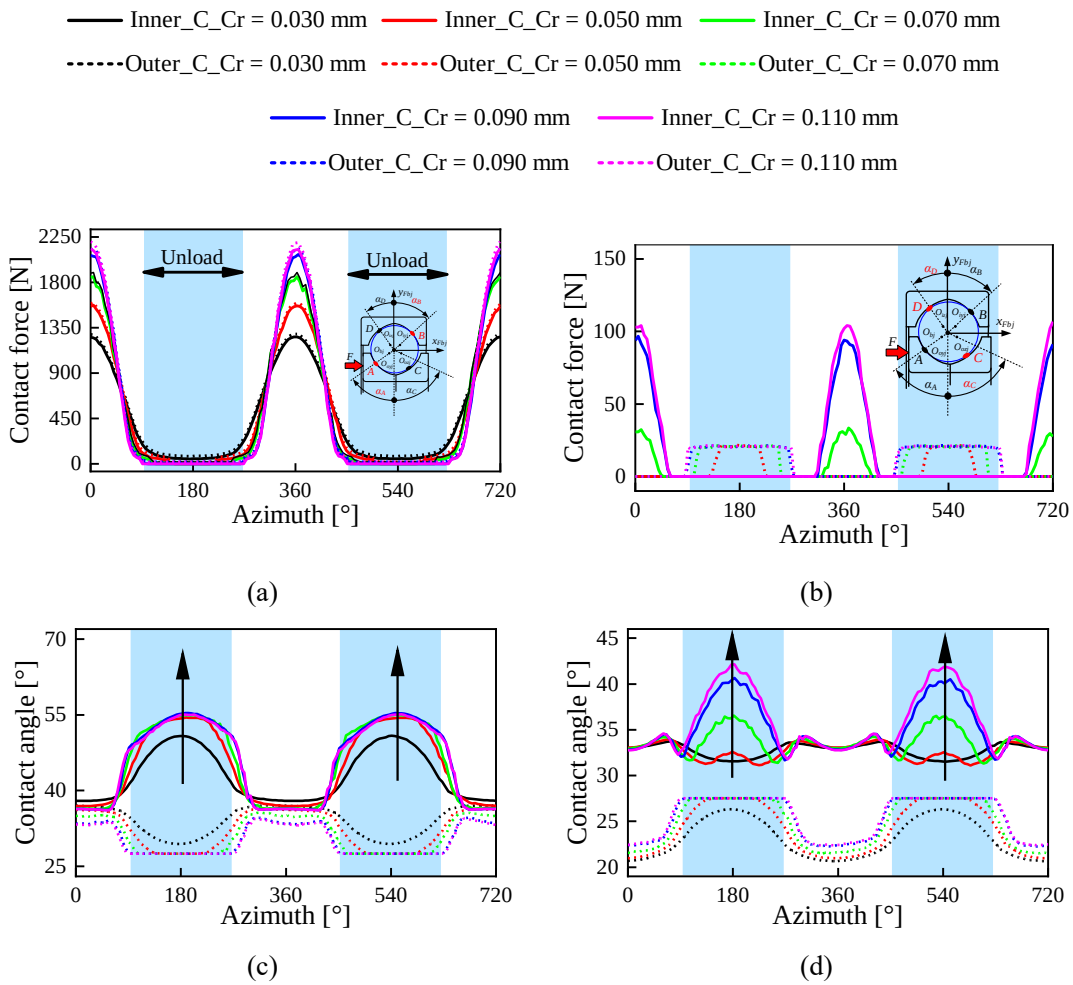

Fig. 27. Effect of CRB clearance on contact feature inside R_FPCBB: (a) load distribution at main-contact pair; (b) load distribution at sub-contact pair; (c) contact angle at main-contact pair; (d) contact angle at sub-contact pair.

Figure 28 further displays the effect of CRB clearance on the sliding feature inside these bearings. As can be seen from **Figs. 28(a)** and **(b)**, the sliding within the loaded zone of L_CRB is slight regardless of the clearance. This indicates that there is no serious sliding within this bearing, which is loss for the bearing life. However, as shown in **Figs. 28(c)** and **(d)**, there is always severe sliding within R_CRB. The severity of the sliding increases as the clearance gradually grows. A similar phenomenon can be observed inside R_FPCBB, presented in **Figs. 28 (e)** and **(f)**. Also, there is an interesting phenomenon in R_FPCBB where the sliding is increasing in the non-load zone. Once the load zoned is reached, the sliding velocity starts to decrease to a minimum value.

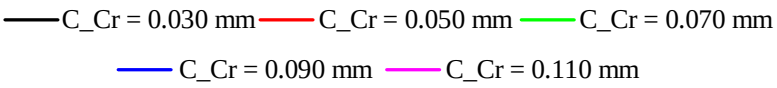

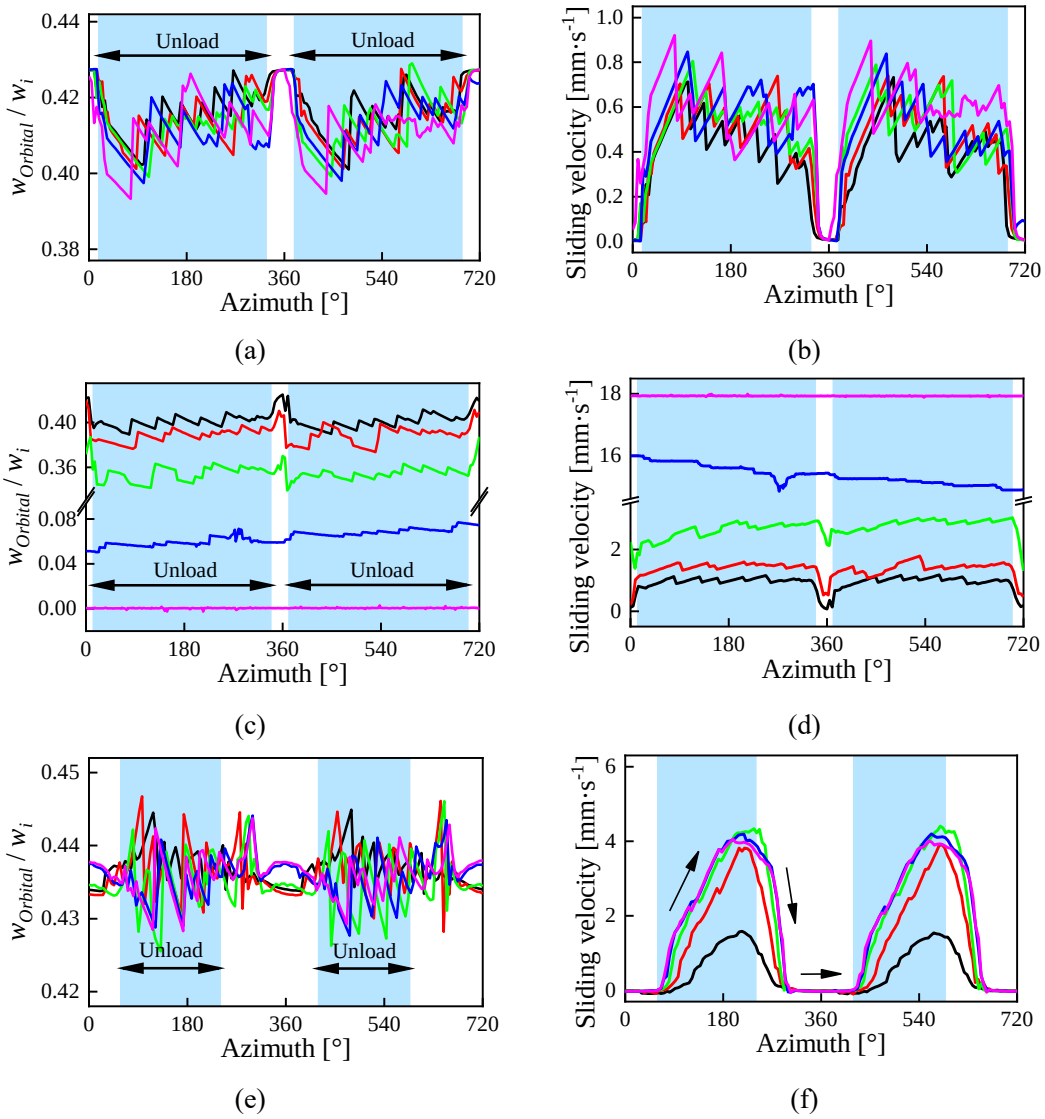

Fig. 28. Sliding features inside the bearing under different CRB clearances: (a) roller's orbital speed (L_CRB); (b) sliding velocity of raceway (L_CRB); (c) roller's orbital speed (R_CRB); (d) sliding velocity of raceway (R_CRB); (e) roller's orbital speed (R_FPCBB); (f) sliding velocity of raceway (R_FPCBB).

Finally, the effect of clearance on the equivalent load and fatigue life of these three bearings is investigated in **Fig. 29**. **Figs. 29(a)** and **(b)** indicates that as the clearance increases, the equivalent load on L_CRB grows while its fatigue life continues to decrease. However, the bearing life feature of R_CRB in **Figs. 29(c)** and **(d)** show the opposite phenomenon. As the serious sliding significantly reduces the bearing fatigue life, its life does not always extend. As shown in **Figs. 29(e)** and **(f)**, similar to L_CRB, the CRB clearance is positive correlated with equivalent load and negatively correlated with fatigue life of R_FPCBB.

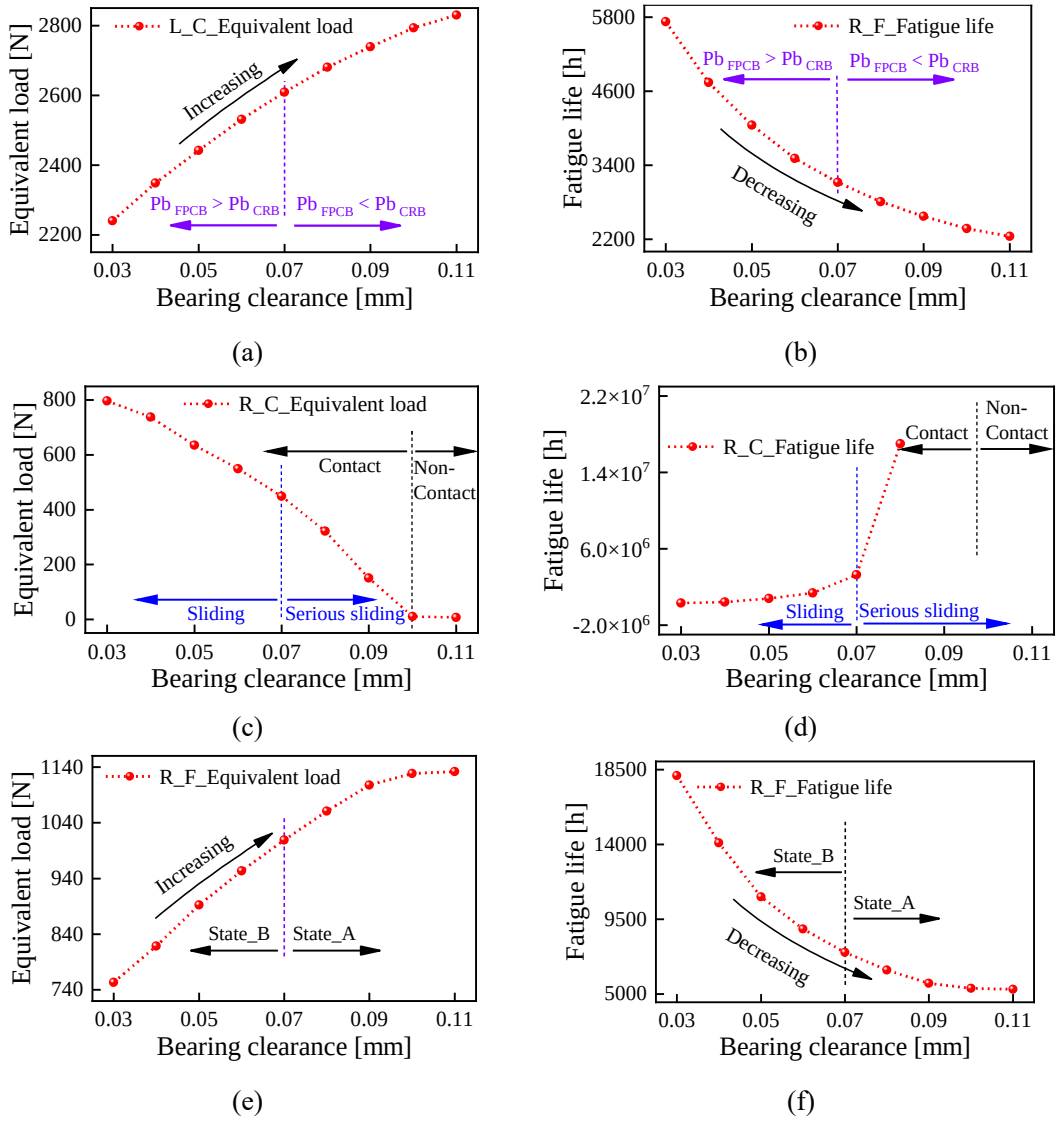

Fig. 29. Effect of CRB clearance on bearing fatigue life: (a) equivalent load (L_CRB); (b) fatigue life (L_CRB); (c) equivalent load (R_CRB); (d) fatigue life (R_CRB); (e) equivalent load (R_FPCBB); (f) fatigue life (R_FPCBB).

Regardless of characteristics, all three bearings are greatly affected by CRB clearance. The life of L_CRB always decreases as the clearance increases, although stress concentrations are mitigated. In the case of R_FPCBB, there is a third contact point, which is detrimental to its fatigue life. Therefore, it is recommended that a smaller CRB clearance be selected to help improve system service performance.

6. Conclusion

Considering the non-inform contact between the roller and other parts, a CRB dynamic model was established by the slice method. Combining the previous works by our team, the dynamic model of the bearing-rotor system covering CRBs and FPCBB in offshore wind gearbox was further presented. The differences between the rigid and flexible models in predicting the system response

were compared. The effects of the bearing clearance on the dynamic behavior of the system were further investigated. The following conclusions were drawn.

(1) Due to the rotor elastic deformation, stress concentrations occur in the raceways of CRB, which can only be sensed by the flexible model.

(2) The wider the clearance, the greater the range of node displacements. And the CRB clearance has a more significant effect on the node displacement of the rotor.

(3) Improper clearance could lead to pronounced sliding on the raceways of CRB, combined with FPCBB.

(4) If it considers the influence of bearing sliding on its fatigue life, the larger the clearance of the CRB, the longer the service life of the bearing-rotor system.

Acknowledgement

This work was funded by the National Outstanding Youth Science Fund Project of National Science Foundation of China (52022077). The authors were grateful for the support of the China Scholarship Council.

Data availability statement

The data that support the finding of this study are available from the corresponding author upon reasonable request.

Conflict of interest statement

The authors declare that they have no known competing financial interests or personal relationships that could have appeared to influence the work reported in this paper.

Reference

[1] Rivera G, Tong V, Hong S. Contact load and stiffness of four-point contact ball bearings under loading. Int J Precis Eng Manuf 2022;23:677-687. https://doi.org/10.1007/s12541-022-00643-0

[2] Leblanc A, Nelias D. Ball motion and sliding friction in a four-contact-point ball bearing. J Tribol 2007;129:801–808. https://doi.org/10.1115/1.2768079

[3] Ma S, He G, Yan K, Li W, Zhu Y, Hong J. Structural optimization of ball bearings with three-point contact at high-speed. Int J Mech Sci 2022;229:107494. https://doi.org/10.1016/j.ijmecsci.2022.107494.

[4] Niu R, Liu Y, Tang H, Cui Y, Deng S. Deformation of the multi-point support structure and loading performance analysis of its shafting bearing. Acta Armamentarii 2023;44(2):615-628. https://doi:10.12382/bgxb.2021.0575

[5] Xu Z, Zhan P, Yang Y. Application analysis on combination of three－point contact ball bearing

and cylindrical roller bearing. Bearing 2015;3:6. https://doi:10.3969/j.issn.1000-3762.2015.03.001.
[6] Stribeck R. Ball bearings for various loads. Trans ASME 1907;29:420-463
[7] Tomovi R. Calculation of the necessary level of external radial load for inner ring support on q rolling elements in a radial bearing with internal radial clearance. Int J Mech Sci 2012;60:23–33. https://doi.org/10.1016/j.ijmecsci.2012.04.002
[8] Liu J, Tang C, Wu H, Xu Z, Wang L. An analytical calculation method of the load distribution and stiffness of an angular contact ball bearing. Mech Mach Theory 2019;142:103597. https://doi.org/10.1016/j.mechmachtheory.2019.103597
[9] Sinha R, Sahoo V. Effect of relative movement between bearing races on load distribution on ball bearings. SN Appl Sci 2020;2:1–12. https://doi.org/10.1007/s42452-020-03833-5
[10] Fang B, Wan S, Zhang J, Hong J. Research on the influence of clearance variation on the stiffness fluctuation of ball bearing under different operating conditions. J Mech Des 2021;143(2):023403. https://doi.org/10.1115/1.4047903.
[11] Xu H, Wang P, Ma H, He D, Zhao X, Bao Y, Yang Y. Contact characteristics analysis of deep groove ball bearings under combined angular misalignments and external loads. J Tribol 2022;144(2):121201. https://doi.org/10.1115/1.4054435
[12] Ma S, Yan K, Li M, Zhu Y, Hong J. Research on the bearing sliding loss based on time-varying contact angle between ball and raceway. Lubricants 2022;10:185. https://doi.org/10.3390/lubricants10080185
[13] Yang Z, Yu T, Zhang Y, Zhang Y, Sun Z. Influence of cage clearance on the heating characteristics of high-speed ball bearings. Tribol Int 2017;105:125–134. https://doi.org/10.1016/j.triboint.2016.09.041
[14] Shi X, Wang L, Qin F. Non-Gaussian surface parameters effects on Micro-TEHL performance and surface stress of aero-engine main-shaft ball bearing. Tribol Int 2016;96:163–172. https://doi.org/10.1016/j.triboint.2015.12.022
[15] Yan K, Wang Y, Zhu Y, Hong J, Zhai Q. Investigation on heat dissipation characteristic of ball bearing cage and inside cavity at ultra high rotation speed. Tribol Int 2015;93:470–481. https://doi.org/10.1016/j.triboint.2015.09.030
[16] Han Q, Chu F. Nonlinear dynamic model for skidding behavior of angular contact ball bearings. J Sound Vib 2015;354:219–235. https://doi.org/10.1016/j.jsv.2015.06.008
[17] Gao S, Chatterton S, Naldi L, Pennacchi P. Ball bearing skidding and over-skidding in large-scale angular contact ball bearings: nonlinear dynamic model with thermal effects and experimental results. Mech Syst Signal Process 2021;147:107120. https://doi.org/10.1016/j.ymssp.2020.107120
[18] Wang Y, Wang W, Zhang S, Zhao Z. Investigation of skidding in angular contact ball bearings under high speed. Tribol Int 2015;92:404–417. https://doi.org/10.1016/j.triboint.2015.07.021
[19] Chen S, Chen X, Shuai Q, Gu J. Effects of cage pocket shapes on dynamics of angular contact ball bearings. Tribol Online 2020;15:343–335. https://doi.org/10.2474/TROL.15.343
[20] Ma S, Yin Y, Zhu L, Yan K, Zhu Y. Dimensional discussion of traction force vector on ball/raceway interface and study of bearing dynamic behavior. J Tribol 2023;45(9):091108. https://doi.org/10.1115/1.4062375
[21] Ma S, Li W, Yan K, Li Y, Zhu Y, Hong J. A study on the dynamic contact feature of four-contact-point ball bearing. Mech Syst Signal Process. 2022;174:109111. https://doi.org/10.1016/j.ymssp.2022.109111
[22] Tu W, Shao Y, Mechefske C. An analytical model to investigate skidding in rolling element

bearings during acceleration. J Mech Sci Technol 2012;26:2451-2459. https://doi.org/10.1007/s12206-012-0627-9
[23] Tu W, Luo Y, Shao Y. Dynamic interactions between the rolling element and the cage in rolling bearing under rotational speed fluctuation conditions. J Tribol 2019;141(9):091101. https://doi.org/10.1115/1.4044082
[24] Tu W, Yu W, Shao Y, Yu Y. A nonlinear dynamic vibration model of cylindrical roller bearing considering skidding. Nonlinear Dyn 2021;103:2299–2312. https://doi.org/10.1007/s11071-021-06238-0
[25] Liu Y, Liu Z, Chen Z, Tang L, Zhai W. Skidding dynamic performance of rolling bearing with cage flexibility under accelerating conditions. Mech Syst Signal Process 2021;150:107257. https://doi.org/10.1016/j.ymssp.2020.107257
[25] Liu Y, Liu Z, Chen Z, Li Y, Zhai W. Dynamic investigation and alleviative measures for the skidding phenomenon of lubricated rolling bearing under light load. Mech Syst Signal Process 2023;184:109685. https://doi.org/10.1016/j.ymssp.2022.109685
[27] Liu Y, Chen Z, Zhai W, Lei Y. Investigation on skidding behavior of a lubricated rolling bearing with fluid–solid-heat coupling effect. Mech Syst Signal Process 2023;206:110922 https://doi.org/10.1016/j.ymssp.2023.110922
[28] Han Q, Li X, Chu F. Skidding behavior of cylindrical roller bearings under time-variable load conditions. Int J Mech Sci 2017;135:203–214. https://doi.org/10.1016/j.ijmecsci.2017.11.013
[29] Han Q, Li X, Yan G, Chu F. Dynamic skidding behavior of skew cylindrical roller bearings under time-variable loads. J Mech Eng 2017;53(9):58–65. https://doi.org/10.3901/JME.2017.09.058
[30] Deng S, Gu J, Cui Y, Sun C. Analysis on dynamic characteristics of cage in high-speed cylindrical roller bearing. Hangkong Dongli Xuebao/Journal of Aerospace Power 2014;29(1):207-215. https://doi.org/10.13224/j.cnki.jasp.2014.01.027
[31] Zhang W, Deng S, Chen G, Cui Y. Study on the impact of roller convexity excursion of high-speed cylindrical roller bearing on roller’s dynamic characteristics. Mech Mach Theory 2016;103:21-39. https://doi.org/10.1016/j.mechmachtheory.2016.04.010
[32] Zhang W, Deng S, Chen G Cui Y. Influence of Lubricant Traction Coefficient on Cage's Nonlinear Dynamic Behavior in High-Speed Cylindrical Roller Bearing. J Tribol 2017;139(61):061502. https://doi.org/10.1115/1.4036274
[33] Deng S, Lu Y, Zhang W, Sun X, Lu Z. Cage slip characteristics of a cylindrical roller bearing with a trilobe-raceway. Chinese J Aeronaut 2018;31(2):351–362. https://doi.org/10.1016/j.cja.2017.07.001
[34] Cui Y, Deng S, Niu R, Chen G. Vibration effect analysis of roller dynamic unbalance on the cage of high-speed cylindrical roller bearing. J Sound Vib 2018;434:314-335. https://doi.org/10.1016/j.jsv.2018.08.006
[35] Liu J, Tang C, Shao Y. An innovative dynamic model for vibration analysis of a flexible roller bearing. Mech Mach Theory 2019;135:27-39. https://doi.org/10.1016/j.mechmachtheory.2019.01.027
[36] Liu J, Li H, Zhang Q, Xiao G. Dynamic simulation of a planet roller bearing considering the cage bridge crack. Eng Fail Anal 2022;131:105849. https://doi.org/10.1016/j.engfailanal.2021.105849
[37] Shi Z, Liu J, Xiao G. Analysis of cage slip and impact force in a cylindrical roller bearing with

race defects. Tribol Int 2022;180:108208. https://doi.org/10.1016/j.triboint.2022.108208
[38] Liu J, Wang L, Shi Z. Dynamic modelling of the defect extension and appearance in a cylindrical roller bearing. Mech Syst Signal Process 2022;173:109040. https://doi.org/10.1016/j.ymssp.2022.109040
[38] Zhang J, Fang B, Zhu Y, Hong J. A comparative study and stiffness analysis of angular contact ball bearings under different preload mechanisms. Mech Mach Theory 2017;115:1-17. http://dx.doi.org/10.1016/j.mechmachtheory.2017.03.012
[40] Liu Y, Chen Z, Wang K, Zhai W. Non-uniform roller-race contact performance of bearings along width in the rotor-bearing system under dynamic loads. J Sound Vib 2022;538:117251. https://doi.org/10.1016/j.jsv.2022.117251
[41] Wang P, Xu H, Ma H, Han H, Yang Y. Effects of three types of bearing misalignments on dynamic characteristics of planetary gear set-rotor system. Mech Syst Signal Process 2022;169:108736. https://doi.org/10.1016/j.ymssp.2021.108736
[42] Wang P, Xu H, Yang Y, Ma H, Duo H, ZhaoX. Dynamic characteristics of ball bearing-coupling-rotor system with angular misalignment fault. Nonlinear Dyn 2022;108:3391–3415. https://doi.org/10.1007/s11071-022-07451-1
[43] Xu H, Yang Y, Ma H, Luo Z, Li X, Han Q, Wen B. Vibration characteristics of bearing-rotor systems with inner ring dynamic misalignment. Int J Mech Sci 2022;230:107536. https://doi.org/10.1016/j.ijmecsci.2022.107536
[44] Li Y, Cao H, Niu L, Jin X. A general method for the dynamic modeling of ball bearing-rotor systems. J Manuf Sci Eng Trans ASME 2015;137. https://doi.org/10.1115/1.4029312
[45] Xi S, Cao H, Chen X. Dynamic modeling of spindle bearing system and vibration response investigation. Mech Syst Signal Process 2019;115:486-511. https://doi.org/10.1016/j.ymssp.2018.05.028
[46] Xi S, Cao H, Chen X, Niu L. Dynamic modeling of machine tool spindle bearing system and model based diagnosis of bearing fault caused by collision. Procedia CIRP 2018;77:614-617. https://doi.org/10.1016/j.procir.2018.08.197
[47] Cao H, Li Y, Chen X. A new dynamic model of ball-bearing rotor systems based on rigid body element. J Manuf Sci Eng Trans 2016;138:1–10. https://doi.org/10.1115/1.4032582
[48] Cao H, Shi F, Li Y, Li B, Chen X. Vibration and stability analysis of rotor-bearing-pedestal system due to clearance fit. Mech Syst Signal Process 2019;133:106275. https://doi.org/10.1016/j.ymssp.2019.106275
[49] Li Y, Cao H, Tang K. A general dynamic model coupled with EFEM and DBM of rolling bearing-rotor system. Mech Syst Signal Process 2019;134:106322. https://doi.org/10.1016/j.ymssp.2019.106322
[50] Wang D, Cao H, Yang Y, Du M. Dynamic modeling and vibration analysis of cracked rotor-bearing system based on rigid body element method. Mech Syst Signal Process 2023;191:110152. https://doi.org/10.1016/j.ymssp.2023.110152
[51] Ma S, Yin Y, Chao B, Yan K, Fang B, Hong J. A real-time coupling model of bearing-rotor system based on semi-flexible body element. Int J Mech Sci 2023;245:108098. https://doi.org/10.1016/j.ijmecsci.2022.108098
[52] Li G, Guo R, Ma Y. Design of a test rig for railroad vehicle gearbox bearings. Railway Quality Control 2022;50:19-22.
[53] Wen C, Meng X, Fang C, Gu J, Xiao L, Jiang S. Dynamic behaviors of angular contact ball

bearing with a localized surface defect considering the influence of cage and oil lubrication. Mech Mach Theory 2021;162:104352. https://doi.org/10.1016/j.mechmachtheory.2021.104352
[54] Zhou Y, Wang X, Hou Y, Que H, Guo R, Lin X, Jin S, Wu C. Test study on vibration behavior and bearing load characteristics of high-speed train gearbox under internal excitation. Journal of Vibration and Shock 2023;42(13):242-250